

# REPORT DOCUMENTATION PAGE

AFRL-SR-BL-TR-98-

Public reporting burden for this collection of information is estimated to average 1 hour per response, including the gathering and maintaining the data needed, and completing and reviewing the collection of information. Send comments regarding this burden estimate or any other aspect of this collection of information, including suggestions for reducing this burden, to Washington Headquarters Services, Directorate for Information Operations and Reports, 1215 Jefferson Davis Highway, Suite 1204, Arlington, VA 22202-4302, and to the Office of Management and Budget, Paperwork Project (0704-0188), Washington, DC 20503.

00601

1. AGENCY USE ONLY (Leave blank)		2. REPORT DATE 10/29/97		3. REPORT TYPE AND DATES COVERED Final Technical Report 04/01/94-08/31/97	
4. TITLE AND SUBTITLE Materials Degradation and Fatigue Under Extreme Conditions				5. FUNDING NUMBERS 61103D 3484 CS	
6. AUTHOR(S) Jiri Jonas					
7. PERFORMING ORGANIZATION NAME(S) AND ADDRESS(ES) Univ of Illinois - Urbana Champaign 801 South Wright Street Champaign, IL 61820-6242				8. PERFORMING ORGANIZATION REPORT NUMBER	
9. SPONSORING/MONITORING AGENCY NAME(S) AND ADDRESS(ES) AFOSR/NC Building 410, Bolling AFB DC 20332-6448				10. SPONSORING/MONITORING AGENCY REPORT NUMBER F49620-93-1-0241	
11. SUPPLEMENTARY NOTES					
12a. DISTRIBUTION/AVAILABILITY STATEMENT APPROVED FOR PUBLIC RELEASE: DISTRIBUTION IS UNLIMITED.				12b. DISTRIBUTION CODE	
13. ABSTRACT (Maximum 200 words)  This AFOSR URI addressed complex research problems of materials degradation and fatigue in aerospace structures in severe or extreme environments. A better understanding of materials degradation and flaw initiation dynamics was achieved through a multi-disciplinary research program encompassing chemistry, surface physics, materials science and mechanics, both experimental and theoretical. The Subprojects were as follows: Surface Induced Degradation of Fluorocarbon Lubricants; Molecular Tribology of Perfluoroether Lubricants; Fluids, Including Lubricants Under Extreme Conditions of High Pressure/High Temperature and Confinement; Surface Crack Propagation Under Combined Mechanical and High Pressure Fluid Loading; Lubricant-Assisted Fatigue Crack Growth in Ceramics.					
14. SUBJECT TERMS lubricants, confined geometries; NMR; laser Raman scattering; high pressure; molecular tribology; surface phenomena; surface crack propagation mechanical loading				15. NUMBER OF PAGES	
				16. PRICE CODE	
17. SECURITY CLASSIFICATION OF REPORT UNCLASSIFIED	18. SECURITY CLASSIFICATION OF THIS PAGE UNCLASSIFIED	19. SECURITY CLASSIFICATION OF ABSTRACT UNCLASSIFIED	20. LIMITATION OF ABSTRACT		

DATA QUALITY IMPROVED 3

Final Technical Report on Grant

AFOSR-F49620-93-1-0241

Period Covered: April 1, 1994 to August 31, 1997

Date: October 1997

University of Illinois

Urbana-Champaign Campus

Urbana, Illinois 61801

PRINCIPAL INVESTIGATOR

Name: Jiri Jonas Department: Chemistry  
Signature: *Jiri Jonas* Address: 166 Roger Adams Lab  
Title: Professor of Chemistry Telephone: (217) 333-2572

**Title: Materials Degradation and Fatigue Under Extreme Conditions**

Sub Projects: Surface Induced Degradation of Fluorocarbon Lubricants; Molecular Tribology of Perfluoroether Lubricants; Fluids, Including Lubricants Under Extreme Conditions of High Pressure/High Temperature and Confinement; Surface Crack Propagation Under Combined Mechanical and High Pressure Fluid Loading; Lubricant-Assisted Fatigue Crack Growth in Ceramics

19980115 216

## TABLE OF CONTENTS

### TECHNICAL SUMMARY

<b>1.0</b>	<b>Research Accomplishments</b> .....	<b>7</b>
<b>1.1</b>	<b>Surface Induced Degradation of Fluorocarbon Lubricants</b> .....	<b>7</b>
<b>1.11</b>	<b>UHV Tribometry</b> .....	<b>7</b>
<b>1.12</b>	<b>Fluoroether Surface Chemistry</b> .....	<b>12</b>
<b>1.13</b>	<b>Fluoroalkoxide Decomposition</b> .....	<b>13</b>
<b>1.14</b>	<b>Fourier Transform Infrared Reflection Absorption Spectroscopy of Adsorbates</b> .....	<b>14</b>
<b>1.2</b>	<b>Molecular Tribology of Perfluoroether Lubricants</b> .....	<b>16</b>
<b>1.21</b>	<b>Nanorheology of Perfluoropolymer Lubricants</b> .....	<b>16</b>
<b>1.22</b>	<b>Concept of Effective Viscosity and Dynamic Viscosity</b> .....	<b>18</b>
<b>1.23</b>	<b>Stiction Phenomenon</b> .....	<b>20</b>
<b>1.24</b>	<b>Hydrodynamic Thickness of Lubricant Additives</b> .....	<b>21</b>
<b>1.3</b>	<b>Fluids, Including Lubricants Under Extreme Conditions of High Pressure, High Temperature and Confinement</b> .....	<b>23</b>
<b>1.31</b>	<b>Dynamic Behavior of Fluids Confined to Nanopores</b> .....	<b>23</b>
<b>1.311</b>	<b>Fluorocarbon Based Fluids</b> .....	<b>23</b>
<b>1.312</b>	<b>Quenched Molecular Reorientation and Angular Momentum for Confined Liquids</b> .....	<b>26</b>
<b>1.313</b>	<b>Dynamics of Complex Phthalate Liquids</b> .....	<b>29</b>
<b>1.4</b>	<b>Surface Crack Propagation Under Combined Mechanical and High Pressure Fluid Loading</b> .....	<b>36</b>
<b>1.411</b>	<b>Experimental Observations under Mixed Mode I/Mode III Loading</b> .....	<b>36</b>
<b>1.412</b>	<b>Governing Equations of a Crack with Surface Friction</b> .....	<b>38</b>

1.413	Solution Method .....	41
1.414	Results.....	42
1.415	Comparison with Experiments.....	44
1.416	Concluding Remarks .....	45
1.42	Efforts of High Pressure Fluid on Surface Crack Growth .....	46
1.421	Theoretical Modeling .....	46
1.422	Experimental Investigation.....	54
1.5	<b>Lubricant-Assisted Fatigue Crack Growth in Ceramics</b> .....	62
1.51	Repeated Indentation Method .....	62
1.52	Surface Crack Studies.....	67
2.0	<b>Publications Acknowledging AFOSR Support</b> .....	72
3.0	<b>List of Personnel</b> .....	78
4.0	<b>Interactions/Transactions</b> .....	80
4.1	Participation/Presentations .....	80
4.2	Consultive/Advisory Functions.....	87
4.3	Transitions.....	87
5.0	<b>Inventions</b> .....	88
6.0	<b>Honors/Awards</b> .....	88

## TECHNICAL SUMMARY

This AFOSR URI on Materials Degradation and Fatigue Under Extreme Conditions addressed complex research problems of materials degradation and fatigue in aerospace structures in severe or extreme environments. A better understanding of materials degradation and flaw initiation dynamics was achieved through a multi-disciplinary research program encompassing chemistry, surface physics, materials science and mechanics, both experimental and theoretical.

The subproject *"Surface Induced Degradation of Fluorocarbon Lubricants"* (A. J. Gellman) aimed at developing a better understanding of the chemistry of fluorocarbon lubricants which lead to their degradation when adsorbed on metal surfaces. A major progress has been made in the understanding of two aspects of the tribological properties of metal surfaces and interfaces. The first is an understanding of the influences of monolayer and submonolayer coverages of adsorbate on friction. This has resulted from friction measurements between extremely highly characterized, single crystalline metal surfaces. The second area of progress was in the understanding of the surface chemistry of fluorinated lubricant fluids. Studies of their surface chemistry have provided insight into the bonding of these molecules to metal surfaces and into the mechanisms and kinetics of their decomposition reactions.

The goal of the work carried out in the subproject *"Molecular Tribology of Perfluoroether Lubricants"* (S. Granick) was the molecular level understanding of fluid flow under extreme conditions of confinement. A key feature was to understand the surface chemical influences of lubrication, as opposed to traditional engineering characterization. The key feature of the experimental approach was to confine fluids between step-free, atomically-smooth surfaces spaced at separations comparable to the size of the molecules themselves. Periodically alternating (AC) shear excitations were applied and the fluid response was quantified in-phase and out-of-phase with the drive.

This allowed a better understanding of the complex interplay between film thickness (resolution  $<0.2$  nm), drive frequency and amplitude, and surface and lubricant chemistry, in determining the ultimate tribological response.

The subproject *"Fluids, Including Lubricants Under Extreme Conditions of High Pressure, High Temperature, and Confinement"* (J. Jonas) focused on the relationship between molecular level properties as obtained for the NMR and laser Raman scattering experiments and the macroscopic properties of the fluids studied, including confined fluids at the fluid-solid interface. Three main projects were pursued: a) development of instrumentation for high pressure NMR experiments; b) NMR relaxation studies of liquids confined to nanopores of silica glasses; and c) dynamic behavior of complex liquids including lubricants.

The combination of high resolution nuclear magnetic resonance (NMR) with high pressure is a valuable technique for probing the dynamic structure of liquids as, for example, it allows separation of the effects of temperature and density on dynamic processes. In this work, two unique high resolution, high pressure NMR probes were developed—a 300 MHz probe which operates in the range of 1 bar to 9 kbar, and a new 500 MHz probe which operates in the range of 1 bar to 5 kbar. Both probes have working temperature ranges of  $-30^{\circ}$  to  $80^{\circ}\text{C}$ .

Dynamic NMR studies at ambient pressure were also performed on the polar fluids ethanol, 2,2,2-trifluoroethanol, propionic acid, and pentafluoropropionic acid confined to porous silica glasses with well-defined pore sizes. The  $^{13}\text{C}$  NMR spin-lattice relaxation times were measured and analyzed in terms of the two-state-fast exchange model, which allowed separation of the surface layer relaxation rates. The experiments showed that the hydrocarbon fluids form stronger hydrogen-bond interactions with the silica surface, and that confinement has little effect on the internal rotation of terminal  $-\text{CF}_3$  or  $-\text{CH}_3$  groups.

In order to interpret the experimental NMR relaxation data a theoretical model for anisotropic molecular reorientation and angular velocity, which accounts for the motional

behavior of non-polar liquids confined to nanopores, was proposed. This model predicted an increase of the reorientational and angular momentum correlation times when the pore size is decreased. Application of this theoretical model to the interpretation of the CS<sub>2</sub> NMR relaxation data and to earlier relaxation results obtained for confined non-polar cyclohexane-d<sub>12</sub> liquid proved successful.

The motional behavior of complex liquids of phthalates have been investigated using <sup>13</sup>C NMR relaxation measurements. The choice of model for spectral density function was critical for the proper analysis of NMR relaxation data in terms of the molecular motion of these complex molecules which have flexible side chains attached to relatively rigid ring structure. In order to select a proper model for the molecular motion of these liquids, natural abundance carbon-13 NMR spin-lattice relaxation time (T<sub>1</sub>), spin-spin relaxation times (T<sub>2</sub>), and nuclear Overhauser enhancements of individual carbons in the complex liquid of di(2-ethylhexyl) phthalate (DEHP) were measured as a function of temperature and pressure. The temperature and pressure effects on the relaxation behavior of DEHP were successfully interpreted in terms of a theoretical model assuming a Cole-Davidson distribution of correlation times and provided the information on overall and internal motions.

Based on the results about DEHP, the effects of structural variation of phthalate liquids in both relatively rigid framework and flexible alkyl side chain on the microscopic motional behavior and macroscopic flow properties were also studied. The <sup>13</sup>C NMR relaxation data analyzed in terms of the Cole-Davidson distribution model provided the detailed information about the effect of the structural change on their motional characteristics. The motional behavior of these compounds were significantly affected by both the structural shape of the framework and the branching of side chain, which was represented by the parameter  $\beta$  in the Cole-Davidson distribution model. The motional characteristics influenced by the molecular structure of the phthalates was related to the macroscopic physical property of viscosity.

The main focus of the subproject "*Surface Crack Propagation and Fatigue Under Extreme Conditions*" (K. J. Hsia, D. F. Socie) was on the investigation of the surface crack growth behavior under combined high hydraulic pressure loading due to lubricants and mechanical loading due to rolling contact. Two thrusts have been actively pursued: the effects of crack surface friction on crack growth behavior, and the effects of high pressure fluid on surface crack growth. Both experimental investigation and theoretical modeling have been conducted.

A mechanistic model has been developed for the surface crack growth in the presence of crack surface friction under mixed mode I/III loading. The material toughening due to crack surface friction was studied. The model takes into account several microstructural and material parameters such as grain shape and friction coefficient between grain boundaries. By employing a self-consistent, fracture mechanics approach, the governing integral equation with a singular kernel was obtained. The numerical solution of the governing equation showed that, because of crack surface friction, the material toughens significantly. Moreover, two parameters, the oblique grain boundary angle and the friction coefficient, have been identified as the controlling parameters for the toughening behavior. The model predictions agreed well with experimental measurements in a ceramic test.

The crack growth under combined external loading and hydraulic pressure have been studied through both experiments and theoretical modeling. The modeling effort focused on the interaction between pressurized viscous fluid and cracked solid. Using fluid mechanics and fracture mechanics method, the governing equations, two coupled integral equations of the fluid pressure distribution and the crack opening displacement, were established. Both an approximate analytical solution and a numerical solution were obtained. The results identified a characteristic penetration time for the fluid-solid system. When the period of the cyclic pressure loading is shorter than the characteristic penetration time, the pressure fluctuations at the crack mouth will not transmit deep into



the crack. Thus the crack growth rate is low. But when the period of the loading is longer than the characteristic time, full penetration of the viscous fluid is expected, resulting high crack growth rate. Full numerical simulations of the crack tip response under different hydraulic pressure loading at the crack mouth have been performed. An experimental apparatus has been constructed which is capable of applying external tension, torsion, and hydraulic pressure loading independently on rod-shaped specimens with surface cracks. Fatigue crack growth rates under both external loading and pressurized fluid loading in light and heavy lubricating oils have been measured. The results confirmed that whether the crack grows or not depends on whether the pressure can fully penetrate deep into the crack. While the crack growth behavior in a light oil is the same as that in air under external loading, the behavior in a heavy oil depends on the loading frequency. Low frequency pressure loading gives rise to full penetration of the pressurized fluid, resulting high crack growth rate. But high frequency loading may not result in any crack propagation at all, as predicted by the theoretical model.

The study represented the first attempt to model and experimentally investigate the complex fluid-solid system with a crack. Its success in predicting qualitatively the crack growth behavior under combined external and hydraulic pressure loading has important implications in material damage in rolling contact components in the Air Force applications. However, further studies are needed to address more realistic systems, including the inclined surface cracks and change of fluid viscosity due to pressure change. These studies will provide guidelines for the material development engineers to come up with new materials and lubricants which will guarantee higher efficiency and safer operation of the next generation of aircraft.

Improvement of our understanding of crack growth in ceramics in contact with lubricants represented the main goal of the research carried out in the subproject "*Lubricant Assisted Fatigue Crack Growth in Ceramics*" (J. K. Shang). This investigation was carried out in four stages. The first stage was aimed at developing the

repeated indentation as a method to determine if a strong interaction exists between lubricants and ceramic materials under contact fatigue and at providing a good understanding of failure processes involved in the repeated indentation method. Using this method, it was found that fluorinated oils interacted strongly with hot-isostatically-pressed  $\text{Si}_3\text{N}_4$  during contact fatigue. Direct observations of the indentation damage showed that the initiation and growth of the lateral cracks led to final surface microfracture. The second stage of the investigation was concentrated on determining the effect of fluorinated oil on fatigue crack growth in the  $\text{Si}_3\text{N}_4$  and on understanding the mechanism underlying such an effect. The fluorinated oil was found to accelerate the fatigue crack growth by reducing the pull-out resistance of elongated grains through grain boundary dissolution and hydrodynamic lubrication. In the third stage of the investigation, attempts were made to determine if the oil degradation, as a plausible explanation to the low oil-pressure build-up inside the fatigue crack and to the strong chemical interaction between the fatigue crack surface and the lubricant, had taken place inside the fatigue crack during cyclic loading. Finally, crack bridging models were developed and compared to the experimental results in order to explain the effect of the fluorinated oil on fatigue crack growth in  $\text{Si}_3\text{N}_4$ .

## **1.0 RESEARCH ACCOMPLISHMENTS**

### **1.1 SURFACE INDUCED DEGRADATION OF FLUOROCARBON LUBRICANTS**

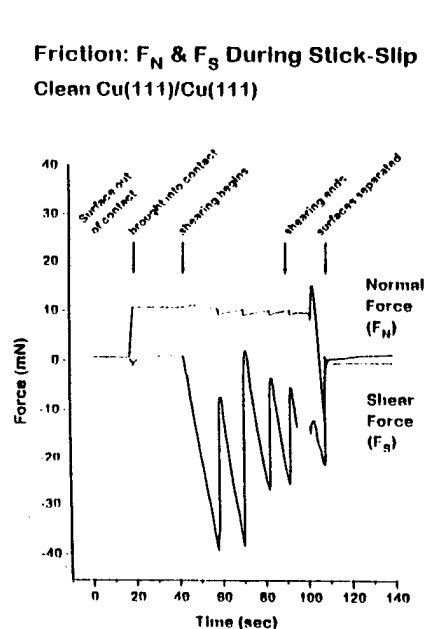
#### **1.11 UHV Tribometry**

The use of UHV conditions for both the preparation of metal surfaces and the measurement of friction between them allows the study of extremely well defined systems and allows us to address fundamental issues in tribology. The UHV tribometer developed in the Gellman laboratory under AFOSR support allows measurement of friction between pairs of metal single crystals whose surfaces have been prepared and characterized to state of the art standards. Friction measurements between the surfaces can be made over a range of sliding conditions including load, sliding speed, temperature, and, of course, surface properties. Our ability to make these measurements is unique and has allowed us to address some hitherto unanswered questions. To date we have made measurements between Ni(100) surfaces, Cu(111) surfaces and the surfaces of  $\text{Al}_{70}\text{Pd}_{21}\text{Mn}_9(00001)$  quasicrystals. These have revealed that while the friction coefficient is independent of the macroscopic sliding conditions (load, temperature, sliding speed) it is critically dependent on the presence or absence of surface species.

The first problem that we have addressed has been that of the influence of adsorbate coverage on friction between metal surfaces. Simply put, how thick a film of adsorbed species is necessary to lubricate a metal-metal interface? The interesting capability of the UHV approach to this problem is that adsorbed films can be produced from a wide variety of species that range in coverage continuously from zero (clean surfaces) to one monolayer to many monolayers in thickness. The UHV approach is the

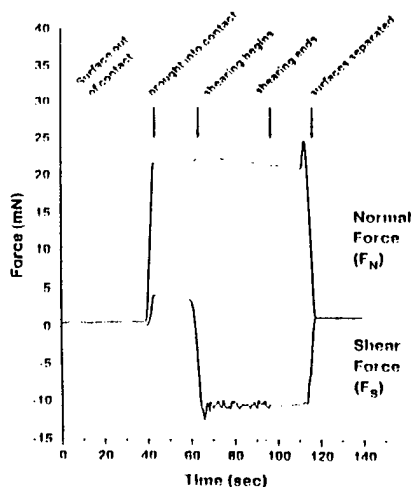
only method of studying the regime of coverages between zero and one monolayer and thus allows us to probe the frictional properties of the virgin metal surfaces that would be produced under sliding contact immediately after wear and removal of an adsorbed lubricant film.

Friction measurements between two surface in UHV are made by bringing the two into contact under an applied normal load, then shearing at a constant rate and then stopping before separating the two surfaces. The type of raw data that is generated by these measurements is shown in Figure 1 which depicts both the normal force and the shear forces during sliding of two Cu(111) surfaces against one another. Figure 1a shows an example of clean surfaces sliding against one another, generating very high coefficients of friction exhibiting obvious stick-slip behavior. When the surfaces are modified by the adsorption of several monolayers of molecular species their behavior (Fig. 1b) is quite different exhibiting smooth sliding and much lower coefficients of friction. This general trend has now been observed in all the systems.



**Fig 1A.** Friction measurement exhibiting "stick-slip" behavior. The negative value of the normal force upon separation is evidence of intermetallic adhesion. Sliding conditions: load  $\approx 10$  mN, shearing velocity =  $3\mu\text{/sec}$ ; temperature = 120K; surface coverage: clean.

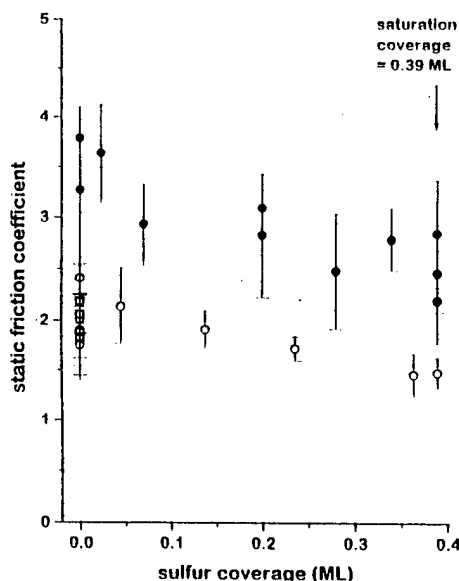
Friction:  $F_N$  &  $F_S$  During Sliding  
Contaminated Cu(111)/Cu(111)



**Fig. 1B.** Friction measurement exhibiting "slip" behavior. The upper trace is a plot of the normal force ( $F_N$ ), while the lower trace is a plot of the shear force ( $F_S$ ). Sliding conditions: load  $\approx 20$  mN; shearing velocity =  $3 \mu\text{m/sec}$ ; temperature = 120 K; surface coverage: 2.25 ML trifluoroethanol.

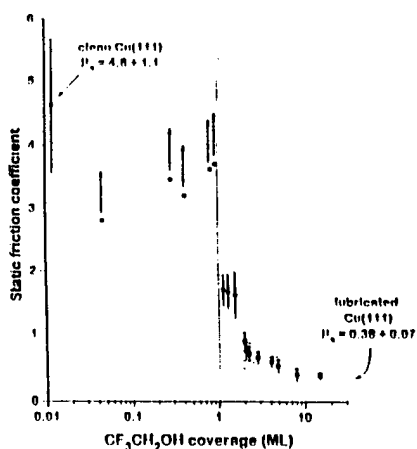
The types of adsorbates used to modify the metal surface used in this work can be divided into two categories: atomic and molecular. The atomic species (S, Cl, I, and O) can be adsorbed on the metal surfaces by various reactions such as dissociation of  $\text{H}_2\text{S}$  or  $\text{Cl}_2$  but in each case can only be adsorbed at coverages ranging from zero to some limiting or saturation value which differs from species to species. All these atomic species form strong bonds with the metal surface. The molecular adsorbates on the other hand adsorb on the surface much more weakly but can be adsorbed at coverages ranging from zero to one to many monolayers. These adsorbates have all been studied by various groups and the coverages, and structures that they form on the surface are well known and have been reproduced in numerous laboratories around the world. Adsorbate coverages are calibrated using fairly standard methods of surface science such as Low Energy Electron diffraction (LEED), Auger Electron Spectroscopy (AES), and thermally programmed desorption (TPD). Figure 2 shows the results of a large set of measurements of friction between Cu(111) surfaces modified by the presence of sulfur at various coverages

## Friction: S/Cu(111) vs. Coverage



**Fig. 2.** Plots of  $\mu_s$  vs. sulfur coverage (relative to the underlying Cu(111) substrate). The sliding conditions were:  $T = 300$  K,  $F_N = 40-70$  mN,  $v_{\text{shear}} = 20$  mm/s (•);  $T = 300$  K,  $F_N = 60-80$  mN,  $v_{\text{shear}} = 20$  mm/s (o). The difference between the two data sets is associated with a remounting of the surfaces accompanied by a change in the relative orientations of the two Cu(111) lattices.

between zero and 0.39 monolayers (saturation). This data is characteristic of the results for all atomic adsorbates and shows quite clearly that the presence of adsorbed atoms at coverages in this range has only a very weak influence on the coefficients of friction between these surfaces. The effects of molecular adsorbates (ethanol, trifluoroethanol, butanol, and heptafluorobutanol) are much more interesting and are illustrated nicely by the results in Figure 3 which plots friction versus coverage for trifluoroethanol adsorbed

Static Friction vs. Coverage  
CF<sub>3</sub>CH<sub>2</sub>OH / Cu(111)

**Fig. 3.** Plot of static friction coefficient vs. trifluoroethanol coverage. Load  $\approx 40$  mN; sliding velocity = 1, 2 or 3  $\mu\text{m}/\text{sec}$ ; temperature = 120 K. Each data point represents the average of 10 friction measurements. The points at coverages less than 1 ML are also averages of 10 measurements but represent lower limits of the static friction coefficient.

on Cu(111) surfaces in the coverage range zero to 15 monolayers. This data is also typical of the results obtained for molecular adsorbates in that they have little effect on the friction coefficient in the coverage range zero to one monolayer but once the monolayer is completed lubrication is observed and the coefficient of friction begins to drop. The operational definition of the monolayer in this case is the coverage at which additional molecules adsorbed on the surface begin to form a second layer and do not interact directly with the metal itself. A schematic synthesis of these results is shown in Figure 4 showing that the friction between clean metal surfaces is high and virtually unaffected by the presence of adsorbate in the coverage range zero to one but begins to decrease immediately once the coverages exceed one monolayer.

4

#### Friction vs. Adsorbate Coverage

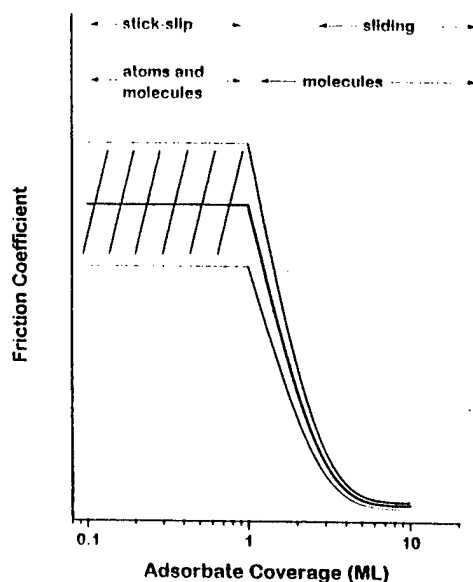


Fig. 4. Schematic summary of the dependence of the friction coefficient between Cu(111) surfaces on adsorbate coverage. The solid line represents the average static friction coefficient and the dashed lines represent the standard deviations normally associated with our measurements.

The unique capability to measure friction between highly characterized metal surfaces is central to further understanding of friction and has been made possible only

through the support of this URI grant. This ability is to be exploited by continuing to address simple, fundamental questions with broad relevance to our understanding of tribology. In parallel with studies of surface chemistry such as those described below we have been able to address problem in the field of lubrication.

### **1.12 Fluoroether Surface Chemistry**

In addition to the development and application of UHV tribology methods concurrent projects have addressed the surface chemistry of fluorocarbons typically used as liquid lubricants under high temperature conditions and under the vacuum conditions of aerospace applications. These fluids are several types of perfluoropolyalkylethers (PFPAEs) which are of interest because of their extremely high thermal stability and their very low viscosity index. The questions that we have addressed are the nature of the interaction of these molecules with metal surfaces and the types of reactions that can lead to their decomposition in the presence of metals. Measurements have been made of the heats of adsorption of several small, model fluoroethers ( $\text{CF}_3\text{OCF}_3$ ,  $\text{CF}_3\text{CF}_2\text{OCF}_2\text{CF}_3$ ,  $\text{CF}_3\text{OCF}_2\text{OCF}_3$ , and  $-\text{CF}_2\text{OCF}_2\text{OCF}_2-$ ) and their hydrocarbon analogs to the surfaces of Cu, Al,  $\text{Al}_2\text{O}_3$ . The consistent picture that has evolved from these measurements and others made in other laboratories is that the bonding of the fluoroethers occurs via dative, electron donation from the oxygen lone pair to the metal surface. More importantly we have been able to observe the dissociation of the fluoroethers on the  $\text{Al}_2\text{O}_3$  surface to deposit fluorine in the form of  $\text{AlF}_3$ . This is one of only two observations that we are aware of the decomposition of these small fluoroethers on well defined surfaces. This observation offers an opportunity to further explore the details of the surface sites and the mechanisms that must lead to the decomposition of the PFPAEs.



The fluoroethers are also used as lubricants on the surfaces of magnetic data storage disks. The work supported by this URI has prompted several collaborative projects and opportunities for technology transfer with companies in the data storage industry. In that field of technology there is an extremely high level of interest in the interactions of the fluoroethers with the amorphous hydrogenated carbon films used to protect the disk surface.

### 1.13 Fluoroalkoxide Decomposition

Our studies of the surface chemistry of fluorinated alcohols has yielded a deep understanding surface chemistry directly relevant to the use of fluorocarbon lubricants. Some classes of the PFPAEs are terminated with alcohol endgroups of the form  $-\text{CH}_2\text{OH}$ . Furthermore, the exploration for possible boundary layer additives for use with the PFPAE fluids has included the investigation of several alcohols. We have focused on understanding the role of fluorination on the thermal stability of alkoxides ( $\text{RCH}_2\text{O}-$ ) formed from alcohols on metal surfaces. These species decompose by a reaction known as  $\beta$ -hydride elimination to yield aldehydes or ketones.



Figure 5 shows the thermally programmed reaction spectra of the decomposition of a set of isopropanoxides on the Cu(111) surface clearly illustrating the fact that the addition of fluorine to the adsorbate results in a dramatic increase in the thermal stability. This result is now known to be quite general to the alkoxides adsorbed on metal surfaces and is understood in terms of a transition state for  $\beta$ -hydride elimination which is truly hydride-

TDS 2-Propanoxides / Cu(111)

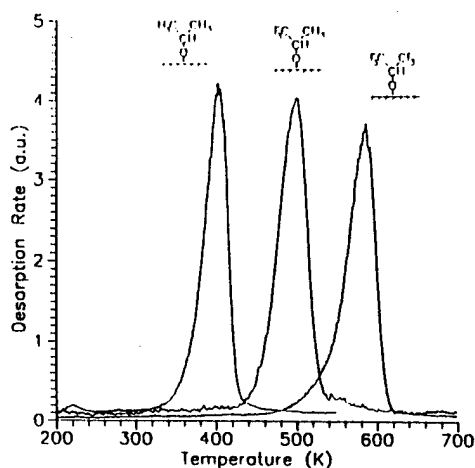


Fig. 5. TPD spectra of the decomposition of isopropanoxides by  $\beta$ -hydride elimination to yield acetone. This is the common mechanism of alkoxides on metal surfaces and the mechanism of alcohol decomposition. Addition of fluorine to the molecule increases thermal stability by energetically destabilizing the transition state to  $\beta$ -hydride elimination.

like  $(RC^{\delta+} \cdots H^{\delta-})$ . Fluorination of the alkyl groups (R) adjacent to the cationic carbon atoms ( $C^{\delta+}$ ) destabilizes this transition state.

#### 1.14 Fourier Transform Infrared Reflection Absorption Spectroscopy of Adsorbates

Fourier Transform Infrared Reflection Absorption Spectroscopy (FT-IRAS) has enabled us to identify reaction intermediates on surface and also to determine adsorbate orientation. Over the past few years we have applied this method to the study of a wide range of fluorocarbons including on metal surfaces. The list includes series of selectively fluorinated compounds such as:

- $CF_3CH_2OH$ ,  $CF_2HCH_2OH$ ,  $CFH_2CH_2OH$ , and  $CH_3CH_2OH$
- $CF_3OCF_3$ ,  $CF_3CF_2OCF_2CF_3$ ,  $CF_3OCF_2OCF_3$ , and  $-CF_2OCF_2OCF_2-$
- $CFH_2CH=CH_2$ ,  $CF_3CH=CH_2$ ,  $CF_3CF=CF_2$ , and  $CH_3CH=CH_2$ .

As an example Figure 6 shows the FT-IRAS spectra of  $CH_3CH_2OH$  and  $CH_3CH_2O$ -adsorbed on the Cu(111) surface. These serve both to identify the adsorbed species by assignment of its vibrational modes and to provide a determination of its orientation

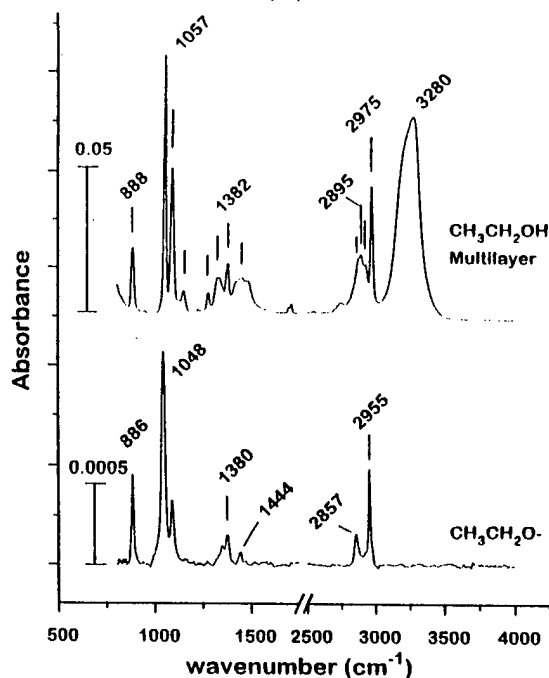
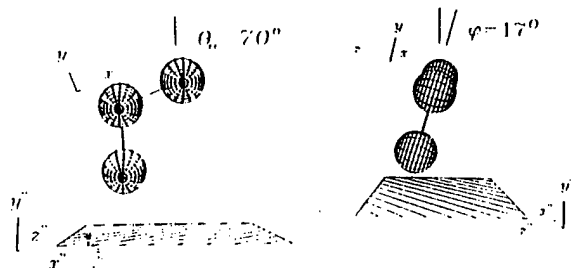


**Fig. 6.** FT-IRAS of multilayer ethanol and ethoxide on Cu(111). Top:  $\text{CH}_3\text{CH}_2\text{OH}$  multilayer, representing  $\sim 20$  ML. 1200 scans of the sample ratioed with 1200 scans of the clean background,  $4 \text{ cm}^{-1}$  resolution,  $\sim 12$  min. Data acquisition time. Bottom:  $\text{CH}_3\text{CH}_2\text{O}_{(\text{ad})}$  5000 sample scans ratioed with 5000 background scans,  $4 \text{ cm}^{-1}$  resolution,  $\sim 24$  min data acquisition time.

through analysis of the intensities of the observed modes. The structures proposed for trifluoroethoxide and ethoxide are shown in Figure 7. This project is providing a deeper understanding of lubricant surface chemistry and is pointing to methods for the future improvement of lubricant formulations.

A)  $\text{CH}_3\text{CH}_2\text{O}_{(\text{ad})}\text{-Cu(111)}$

7



B)  $\text{CF}_3\text{CH}_2\text{O}_{(\text{ad})}\text{-Cu(111)}$

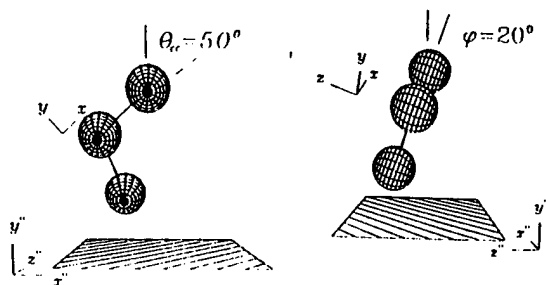


**Fig. 7.** Comparison of the orientations of ethoxide and trifluoroethoxide on Cu(111). For the quantitative determination of  $\text{CH}_3\text{CH}_2\text{O}_{(\text{ad})}/\text{Cu(111)}$  orientation (A), angles are  $\theta_{\text{CC}} = 70 \pm 2^\circ$ ,  $\theta_{\text{CO}} = 17 \pm 2^\circ$ . For the quantitative determination of  $\text{CF}_3\text{CH}_2\text{O}_{(\text{ad})}/\text{Cu(111)}$  orientation (B), angles are  $\theta_{\text{CC}} = 50 \pm 5^\circ$ ,  $\theta_{\text{CO}} = 20 \pm 11^\circ$ .

## 1.2 MOLECULAR TRIBOLOGY OF PERFLUOROETHER LUBRICANTS

### 1.21 Nanorheology of Perfluoroether Lubricants

To understand the dependence of nanorheology on molecular architecture for perfluorinated molecules, studies were performed using two lubricants commonly of interest to the Air Force for high temperature lubrication applications. Experiments mimicked a single asperity by confining liquids to molecular spacings between atomically smooth mica and applying oscillatory shear forces. The force-distance profiles were compared. Large differences were obtained for the linear shear response. The elastic and dissipative shear moduli of a branched perfluoropolymer (Krytox-AZ) were comparable even at high loads, signifying that the fluid remained fluid-like over experimental frequencies. However, linear perfluoropolymer (Demnum S-20) was easily solidified. The nonlinear responses were also surprising. Previously, we reported that the shear-induced transition from an elastic state (at rest) to a dissipative state (during sliding) was discontinuous and hysteric for various hydrocarbon fluids but not for the perfluorinated chain, perfluoroheptaglyme. However, the stick-slip transition was discontinuous, and even more hysteretic for the linear perfluoropolymer (Demnum S-20). Other model PFPAE fluids were also investigated. An example of the differences between different fluids is shown in Fig. 8:

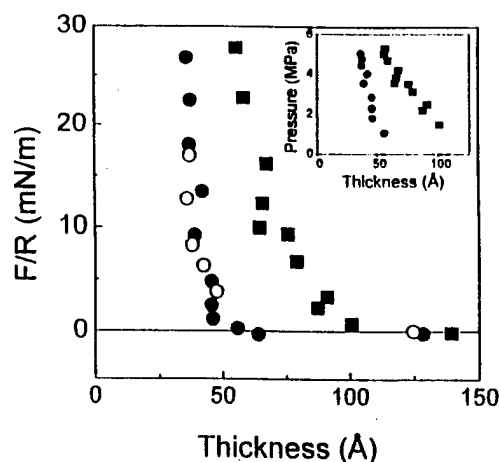


**Fig. 8.** The static force,  $F$ , normalized by the mean radius of curvature,  $R$ , of the crossed cylindrical surfaces plotted against the liquid film thickness. Inset: pressure-thickness relation for Demnum-S20 and Krytox-AZ. Squares, Demnum-S20 and Circles, Krytox-AZ. Filled circles denote measurements during compression and open circles denote measurements made during increase of the films thickness.

In order to generalize this findings to achieve predictive power in situations where detailed experimentation is not feasible, a new friction map was constructed. Recent advances in measuring the rheology and tribology of thin liquid films between shearing surfaces have enabled previously-inaccessible parameters to be accurately measured during frictional sliding. These include the real area of contact, the local asperity load and pressure, and the sheared film thickness. The results show striking non-continuum, non-bulk like effects when the thicknesses of sheared films approach molecular dimensions as occurs under most tribological conditions. Based on these new results, we assessed the validity of current presentations of friction processes, such as the Stribeck curve, and propose new constitutive relations and a dynamic friction map, including an alternative Stribeck type curve representation, which are also formulated in terms of more accessible parameters.

In order to further investigate origins of static friction and "stiction", a simple globular-shaped liquid (octamethylcyclotetrasiloxane, OMCTS) was placed between two solid plates at variable spacings comparable to the size of this molecule and the linear shear viscoelasticity of the confined interfacial film was measured (see Fig. 9). Strong monotonic increase of the shear relaxation time, elastic modulus, and effective viscosity were observed at spacings less than about 10 molecular dimensions. Frequency dependence showed good superposition at different film thickness. The observed smooth transition to solidity is inconsistent with a first-order transition from bulk fluid to solidity.

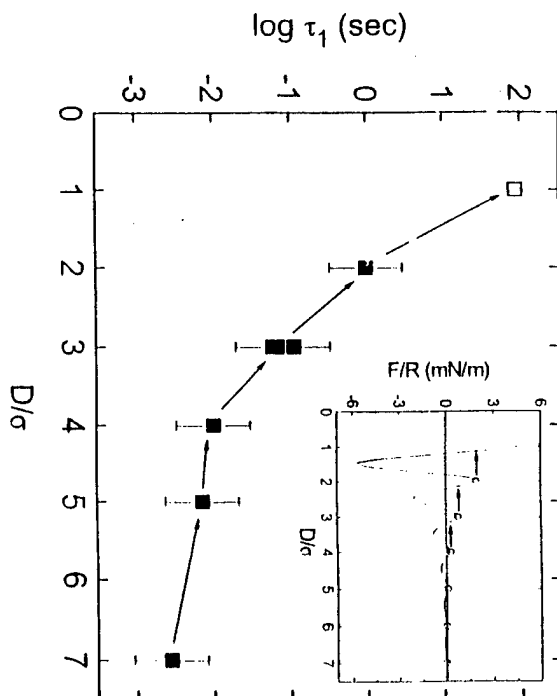


**Fig. 9.** Longest relaxation time plotted logarithmically against film thickness expressed in multiples of the molecular dimension of OMCTS. Data at different thickness were acquired by squeezing the surfaces together progressively as shown in the Inset. Inset shows the force,  $F$  (normalized by the radius of curvature of the mica sheets,  $R$ ) required to squeeze the films to the given thickness. As the normal force was increased beyond the values indicated by circles, film thickness decreased abruptly by the thickness of a single molecule, as indicated schematically by the arrows. Open square: extrapolated measurement. Filled squares: measured values.

## 1.22 Concept of Effective Viscosity and Dynamic Viscosity

Thus, it became clear that knowledge of the bulk viscosity provides little guidance to predict accurately the interfacial shear strength and effective viscosity of a fluid in a lubricated contact. The effective shear viscosity in a thin film is enhanced compared to the bulk, relaxation times are prolonged, and nonlinear responses set in at lower shear rates. These effects are more prominent, the thinner the liquid film. Studies with lubricant additives cast doubt on the usefulness of the concept of friction coefficient for lubricated sliding. To quantify the effective viscosity, a useful measure was the dynamic viscosity. The dynamic viscosity, measured when a surface is sheared in oscillatory displacement, is the peak shear stress during a cycle, divided by peak shear rate. The dynamic viscosity has two components: a dissipative component,  $n'$ , that is in-phase with the shear rate, and an elastic component,  $n''$ , that is in-phase with the displacement amplitude. In Fig. 3A, the effective viscosity of Krytox-AZ is plotted against shear frequency on log-log plots. Fig. 3B contrasts the response of Demnum S-20. The normal load was small -- 4 MPa or less.

less. The data show clearly that the response was non-Newtonian in both cases. The data also show clear differences between the two lubricants. The elastic component of effective viscosity dominated for Demnum S-20, whereas it was less by orders of magnitude for Krytox-AZ. Detailed consideration shows that this is correlated with stiction behavior in the former case, but smooth start-up of sliding in the latter case. Measuring the frequency dependence of the dynamic viscosity thus permits one to predict the occurrence (or not) of stiction behavior.

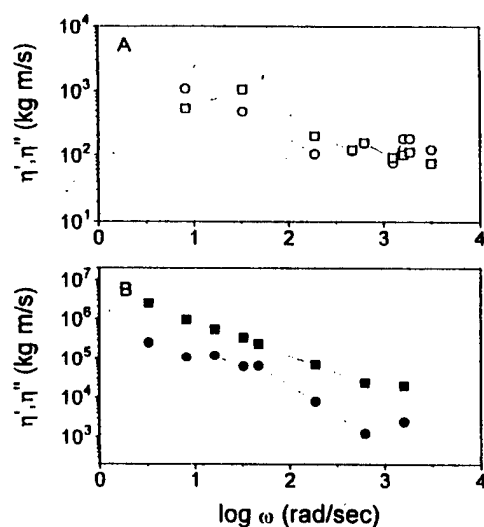


**Fig. 10.** Comparison of Krytox and Demnum at molecularly-thin spacings between solid surfaces. The viscosity of these fluids is dramatically different although nearly the same, 0.744 poise (Krytox-AZ) or 0.781 poise (Demnum S-20) in the bulk. Dynamic viscosity is plotted against frequency. Circles denote the dissipative response (in-phase with the shear rate). Squares denote the elastic response (in-phase with the shear amplitude). Top panel (open symbols): Krytox-AZ. Bottom panel (filled symbols): Demnum S-20.

Shear rate can be approximated, for large amplitudes of sinusoidal displacement, to be the product of oscillation amplitude and oscillation frequency. It is of especial interest to consider the dependence of effective viscosity on shear rate for perfluoropolyether fluids. In **Fig. 11**, effective viscosity plotted against effective shear rate on log-log scales. The data refer to the above-mentioned sample of Demnum S-20. Data from two experiments are shown: one at 1.3 Hz, the other at 200 Hz. The closed symbols represent data taken with increasing strain and the open symbols data taken with decreasing strain. In the stick regime, the effective viscosity was constant. After the

stick-slip transition from the elastic to the dissipative state, shear thinning was observed. The effective viscosity decreased as a power law in the shear rate, with slope increasing in magnitude (from  $-2/3$  to  $-1$ ) with increasing shear rate. At higher shear rates, as the limiting shear stress of the lubricant is approached, the power-law of shear thinning approached the slope of  $-1$ , indicating that the dissipative shear stress reached a limiting plateau.

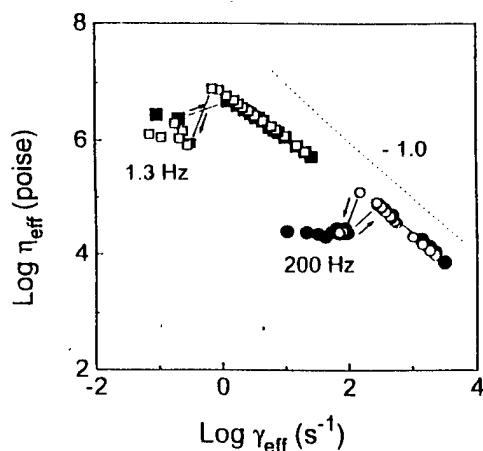


**Fig. 11.** Effective viscosity of Demnum S-20 plotted against the effective shear rate at two frequencies, 1.3 and 200 Hz. In the stick regime, the effective viscosity was constant. After the stick-slip transition from the elastic to the dissipative state, shear thinning was observed. The effective viscosity decreased as a power law in the shear rate, with slope  $-2/3$  at moderate shear rate and  $-1.0$  at sufficiently large shear rate. Interestingly, the data of the two experiments at two different frequencies.

### 1.23 Stiction Phenomenon

The stiction phenomenon was further investigated. With displacements controlled from sub-nanometers to macroscopic distances, we studied friction of atomically smooth solids separated by molecularly-thin films of liquid or grafted monolayers. The method involved a surface forces apparatus with oscillatory shear attachment. To initiate sliding it was necessary to overcome an elastic state whose modulus, deformability, and yield stress were rubber-like in magnitude and remarkably low. This transition was typically (but not under all circumstances) discontinuous. The regime of sliding motion showed a wide range of velocity in which dissipative stress was nearly velocity-independent. The physical mechanism may involve wall slip.



Later we came to doubt that textbook claim that friction is a well-defined, exact number. The textbooks state that solid surfaces, when impelled to slide over one another, remain at rest until a friction force is overcome; after this the velocity determines the force that resists sliding. Various "friction-velocity" models have been considered in the literature. Parallel to this dogma is the experience, familiar to all who make measurements, that fluctuation and irregularity are endemic whenever friction is actually measured. Mundane features of sample inhomogeneity are the usual presumed explanation. In a series of studies we reported friction fluctuations in a system largely free of this concern (atomically smooth mica lubricated by molecularly-thin films of squalane). Millions of repetitive cycles of sinusoidal force were applied without wear. During each cycle the surfaces passed from relative rest to sliding motion. The kinetic friction showed a broad power law distribution of fluctuation size and duration with correlations lasting for many periods of applied force. The distribution was quantified.

#### **1.24 Hydrodynamic Thickness of Lubricant Additives**

Rather than only concentrate on shear response, hydrodynamic drainage in the presence of polymer additives was also studied. Small-amplitude oscillatory displacements in the normal direction were used to measure the drainage of tetradecane (a good solvent) past polybutadiene (PB) brushes end-attached to two opposed mica surfaces. The PB was attached by selective adsorption of the polyvinylpyridine (PVP) block of a PB-PVP diblock copolymer. In-phase motion in the normal direction reflected elastic forces; these were found to be equivalent to the static force-distance profile measured directly. Out-of-phase motions reflected viscous flow of solvent since the PB chains did not contribute to dissipation over the oscillation frequencies studied. No frequency dependence was

observed from 1 to 100 Hz. The hydrodynamic forces at a given plate separation ( $D$ ) implied an effective plate separation less than  $D$  by a constant hydrodynamic thickness ( $R_H$ ) but otherwise the flow of a Newtonian liquid with viscosity same as in the bulk. The value of the hydrodynamic thickness was less than the value ( $L_0$ ) measured in the equilibrium force-distance profile, implying significant penetration of the velocity field into the brush layer. The value of  $R_H$  diminished monotonically as the plate separation was reduced from  $4L_0$  to  $0.2L_0$ . In other language, the "slip plane" changed monotonically with decreasing film thickness. The magnitude of hydrodynamic forces grew in proportion to  $D^{-1.2}$ . This would be expected from scaling arguments for a theta solvent but deviates decidedly from the predicted  $D^{-0.5}$  from scaling arguments for semi-dilute good solvent conditions. This could reflect inapplicability of the Brinkman equation or could reflect different scaling behavior of the static and hydrodynamic screening lengths.

Finally, a program of experimentation directed towards understanding the nanotribology of molecules relevant to lubrication additives was initiated. The friction of molecularly-thin fluids of very different structure were contrasted: a globular molecule, branched alkanes, and a polymer brush in near-theta solution (polystyrene-polyvinylpyridine). In each case the data suggest a prolongation of the longest relaxation time with increasing compression. At frequencies longer than the inverse relaxation time the shear response was "solid-like" but at lesser frequencies it was "liquid-like."

### **1.3 FLUIDS, INCLUDING LUBRICANTS UNDER EXTREME CONDITIONS OF HIGH PRESSURE, HIGH TEMPERATURE AND CONFINEMENT**

#### **1.31 Dynamic Behavior of Fluids Confined to Nanopores**

In view of its importance in studying fundamental aspects of molecular dynamics and its relevance to technological applications, it is not surprising to find that the study of liquids in confined geometry is continuing to receive a considerable amount of attention. In the last several years, the systematic work performed in our laboratory by using NMR relaxation has been aimed at a more complete understanding of the effect of geometrical confinement on reorientational and translational behavior of liquids confined to well characterized nanopores in silica sol-gel glasses.

##### **1.311 Fluorocarbon Based Fluids**

We investigated the role of fluorine in modifying the dynamic behavior of fluorocarbon-based fluids in porous silica glasses. It has been well known that fluorocarbons have much higher thermal stability and chemical inertness compared to their parent hydrocarbons. Fluorination improves greatly the quality of lubricants or greases used at high-temperature and other extreme conditions. In a real engine, boundary layer lubricant additives interact with an oxide-coated surface to form a molecular layer film, which prevents direct contact between metal parts. A main objective of our research was to investigate the effect of fluorination on the behavior of fluids near solid/fluid interfaces at the microscopic level. This provided insight into the surface layer dynamics relevant for boundary layer lubrication and the information regarding potential additives soluble in fluorocarbons.

Our earlier NMR relaxation studies of molecular liquids in silica glasses provided the theoretical background for this investigation. In order to study the solid-liquid interface phenomena by NMR, one must separate the NMR signal from molecules in both bulk and surface layers. For a polar liquid confined to high-purity silica glasses, the observed spin-lattice relaxation rate ( $T_1^{-1}$ ) is affected mainly by the interaction of the confined liquid with the glass surface. Thus the relaxation may be described by the two-state, fast exchange model,

$$\frac{1}{T_1} = \frac{1}{T_{1b}} + \frac{2\varepsilon}{R} \left[ \frac{1}{T_{1s}} - \frac{1}{T_{1b}} \right], \quad (1)$$

where  $T_{1b}$  and  $T_{1s}$  are the bulk and surface layer spin-lattice relaxation time, respectively,  $\varepsilon$  is the thickness of the surface layer (usually assumed equal to two molecular diameters), and  $R$  is the average pore radius. As Equation (1) shows, one can determine the relaxation rate of the surface-layer liquid by measuring the relaxation rates over a range of pore radii. Moreover, the surface enhancement factor,  $T_{1b}/T_{1s}$ , which emphasizes the relative differences in relaxation rates due to the surface, indicates the strength of the surface interaction affecting the motional dynamics of surface-layer liquid.

Two studies in our laboratory investigated polarity-related fluorine effects on the motional behavior of liquids near a silica surface. For methylcyclohexane (MCH), we found that perfluorination strengthens the interaction of the confined liquid with the glass surface. This is because, although MCH shows no molecular dipole moment, local C-H bonds of MCH still interact with the surface. Fluorination increased the bond dipole moment of C-F, and thus increased the local surface interaction. In contrast, for polar ethanol (EtOH) which acts as a hydrogen bond acceptor and forms a strong hydrogen bond with OH groups on the silica surface, the opposite trend was observed. The decrease in surface interaction for trifluoroethanol versus EtOH can be readily explained by the electronegative fluorine substituents withdrawing electron density from the oxygen atom

thus weakening the hydrogen bond. These observations strongly suggested that the effects of fluorination on the dynamics of surface liquids are related the nature of the liquid studied and the way the liquid interacts with the surface.

A dynamic nuclear magnetic resonance (NMR) study of the polar liquids pyridine and pentafluoropyridine (PFP) confined to porous silica sol gel glasses was also carried out. This study was performed with the primary goal of examining fluorine-modified rotational anisotropy of liquids at solid/liquid interfaces, and represented a continuation of our efforts to examine the role of fluorine in modifying the dynamic behavior of molecular liquids. For  $^{13}\text{C}$  NMR, intra-molecular dipole-dipole interaction usually dominates the relaxation times. Therefore, the rotational anisotropy of a molecule can be evaluated by examining the relaxation of carbon atoms at different molecular positions. It is known that the electronegative fluorine substituent makes pyridine a weaker hydrogen bond acceptor. Since pyridine serves as the hydrogen bond acceptor in the interaction with OH groups on the glass surface, we expected fluorination to weaken the interaction of pyridine with the silica surface.

The  $^{13}\text{C}$  NMR spin-lattice relaxation times,  $T_1$ , of ortho (C2), meta (C3), and para (C4) carbons were measured in glasses with pore radii ranging from 30 to 94 Å, over a temperature range of -22°C to 20°C. The experimental data was analyzed in terms of the two-state, fast exchange model, and the surface-layer relaxation times,  $T_{1s}$ , were calculated. Based on surface enhancement factors,  $T_{1b}/T_{1s}$ , where  $T_{1b}$  is the relaxation time of the bulk liquid, we conclude that fluorination considerably weakens the interaction of pyridine with the glass surface. This is consistent with pyridine serving as a hydrogen bond acceptor for the surface. By analyzing the relaxation differences, in C2, C3 and C4, we found that the reorientation of confined pyridine is highly anisotropic, due to directional hydrogen bonding between the N atoms of pyridine and the OH groups on the glass surface.

### 1.312 Quenched Molecular Reorientation and Angular Momentum for Confined Liquids

The confinement of molecular liquids to porous media causes dramatic changes in their dynamic properties. Due to the particular sensitivity of NMR relaxation to the rotational and translational motions of molecules, it was not surprising to find that nuclear relaxation techniques had been successfully applied to investigate the effects of confined geometry on the dynamics of liquids. The common NMR relaxation features for liquids in porous media include: (i) The spin-lattice relaxation time  $T_1$  is markedly decreased compared to the values in the bulk liquid; and, (ii) The spin-spin relaxation time  $T_2$  is smaller than  $T_1$ , even in the motionally narrowed regime ( $\omega\tau \ll 1$ ).

The first theoretical model used to explain the relaxation behavior for confined liquid is the so-called two-state, fast-exchange model. According to this model, the observed reduction of the relaxation times was due to the interaction between liquid and the solid surface, which hindered the molecular motion and thus enhanced the nuclear relaxations. In the absence of surface interaction, as was the case for non-polar liquids, the two-state model lacked physical meaning and the enhancement of the relaxation rate of the confined liquid was mainly due to pure topological restrictions. For example, the translational diffusion of a liquid in pores was obviously different from that of the liquid in bulk because of the boundary effect at the solid/liquid interface. Such topological confinement lowered the dimensions quality of the system. The forward and backward molecular motions enhanced the probability of molecular reencounter, and thus the intermolecular nuclear dipole-dipole relaxation rates. In addition, the topological effect

can also influence the rotational anisotropy of molecular liquids, which may lead to a more complicated relaxation behavior for confined liquids.

So far all NMR studies of the dynamics of liquids in confined geometries followed nuclei relaxed either by dipolar or quadrupolar relaxation mechanisms, thus giving information on reorientational and translational motions. However, angular momentum relaxation of small molecules as determined from NMR relaxation times contributed to our understanding of molecular dynamics both in the liquid and gaseous states. The angular momentum correlation time,  $\tau_{\text{jb}}$ , is the average time a molecule needs to lose memory of its initial angular momentum. One would expect  $\tau_{\text{jb}}$  to be closely related to the time between collisions which randomize the initial angular momentum. In the NMR experiment  $\tau_{\text{jb}}$  can be directly determined from the spin-lattice relaxation time of a nucleus which is relaxed by spin-rotation interaction mechanism. Therefore, one can expect that a study of angular momentum relaxation for liquids in confined geometry will provide new information related to their rotational behavior.

In this study, the spin-lattice relaxation times of natural abundance  $^{13}\text{C}$  of nucleus carbon disulfide ( $\text{CS}_2$ ) confined to porous silica glasses, were investigated as a function of pore radius in the range from 15Å to 102Å over the temperature range of 168°K to 293°K. As a linear molecule with no dipole moment,  $\text{CS}_2$  does not interact with the glass surface and thus the effects from surface interaction can be neglected. The most distinguishing feature of this study was that the  $^{13}\text{C}$  relaxation of  $\text{CS}_2$  in bulk or in pores were dominated by the spin-rotation interaction near room temperature, which was different from those in earlier studies where quadrupolar or dipolar interactions played an important role in the nuclear relaxation.

For liquids undergoing isotropic molecular reorientation, the relaxation rate due to spin-rotation interaction is given by

$$\frac{1}{T_1^{\text{SR}}} = \frac{2\pi I k T}{\hbar^2} C_{\text{eff}}^2 \tau_{\text{Jb}} \quad (2)$$

where the spin-rotation constant  $C_{\text{eff}}^2$  is  $C_{\text{eff}}^2 = (2C_{\perp}^2 + C_{\parallel}^2)/3$ , and  $\tau_{\text{Jb}}$  is the angular momentum correlation time. Other symbols have their usual meaning. In the diffusion limit,  $\tau_{\text{Jb}}$  is related to the molecular reorientation correlation time  $\tau_{\text{b}}$  by the Hubbard equation:

$$\tau_{\text{b}} \tau_{\text{Jb}} = I / 6k T \quad (3)$$

where  $I$  is the moment of inertia.

The  $^{13}\text{C}$  spin-lattice relaxation behavior of bulk liquid  $\text{CS}_2$  has been studied by Spiess and co-workers over the temperature range of 108°K to 167°K at resonance frequencies of 13, 30, and 62 MHz. They found that the relaxation is caused mainly by spin-rotation at high temperature, and by anisotropic chemical shift at low temperature. The dipolar contribution to  $1/T_1$  is less than  $10^{-5} \text{ sec}^{-1}$ , which can be neglected compared with the measured relaxation rates. Changing the temperature varies the proportions of these two mechanisms in the whole relaxation process. Using the expression of relaxation due to an anisotropic chemical shift

$$\frac{1}{T_1^{\text{CS}}} = \frac{2}{15} \omega^2 (\Delta\sigma)^2 \tau_{\text{b}} \quad (4)$$

(where  $\Delta\sigma$  is the anisotropic chemical shift), as well as Eq. (2) and Eq. (3), Spiess et al. separated the contributions from spin-rotation and anisotropic chemical shift and quantitatively determined the spin-rotation constant  $C$  ( $C = C_{\perp}$ , note that  $C_{\parallel}$  vanishes for a



linear molecule), the anisotropy of the chemical shift  $\Delta\sigma$ , and the correlation times for angular velocity  $\tau_b$  and angular reorientation  $\tau_b$  in  $\text{CS}_2$ .

As already mentioned the effects of confinement in nanopores have contributions that originate from the restricted dynamics and surface interactions. Since the surface interactions are very weak for nonpolar confined liquids only the restricted dynamics play a role. However information on this dynamics can be obtained provided that one can answer the following theoretical question: how do the reorientational and angular velocity correlation times of this confined liquid depend on the average pore size? The aim of this study which outlines the dynamics of confined non-polar fluids was two-fold; (i) We addressed the theoretical question and proposed a model for quenched reorientations and angular velocity in restricted geometries. (ii) We compared this theory to experimental pore size dependences of longitudinal relaxation rates of different nuclei on carbon disulfide and cyclohexane liquids in a set of calibrated nano-porous silica glasses.

### **1.313 Dynamics of Complex Phthalate Liquids**

The purpose of the study of dynamic structure of complex liquids including lubricants is to understand the detailed picture of the molecular motion of the fluids in molecular level and consequently to improve the understanding the lubrication process as well as molecular interactions which is responsible for the materials degradation and flaw initiation.

We chose a series of phthalates and the related compounds with similar structure as a model system for our study. These compounds comprise industrially very important molecules and are used widely as general-purpose plasticizers, synthetic lubricants, and vacuum pump fluids. Generally, the structural variation of compounds imparts significant

effects on their physical properties. Hence, by studying and comparing the properties of these compounds, one can know the effect of the structural change on the performance characteristics such as the compatibility, the viscosity (and the viscosity index) and the mechanical properties, and predict the physical properties of the compound of the related structure.

The compounds investigated in this study can be divided into two groups. In Group 1, all the compounds have 2-ethylhexyl ester side chain in common. The chemical structures of the Group 1 compounds are shown in Figure 12.

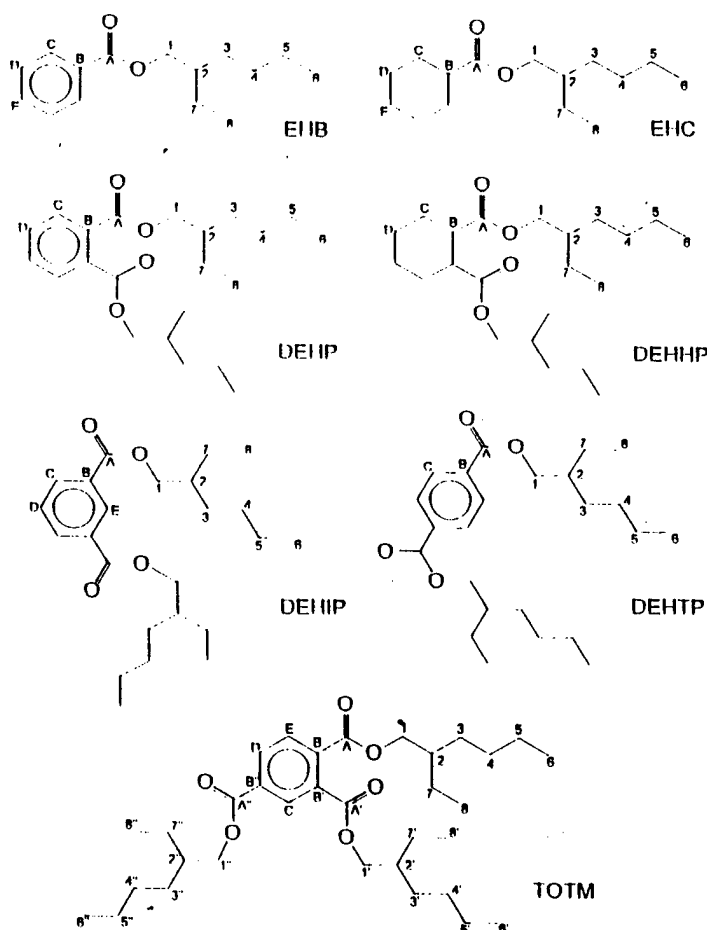


Figure 12

By comparing the dynamic behavior of these compounds, the effect of structural changes

in the ring part of the molecules and the changes of the number of the substituents were elucidated.

Group 2, included the compounds of different phthalates with various side chain, of which the molecular structure is shown in Figure 13.

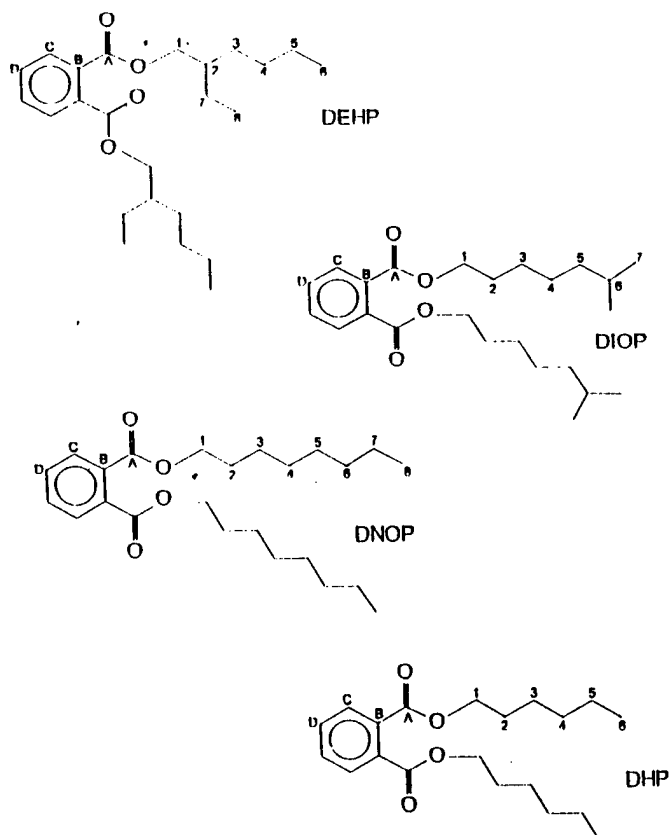


Figure 13

In this case the focus is the effect of the changes of the side chain on the dynamic properties of these functional fluids. In this study the motional behavior of these fluids of complex structure has been studied through physical property measurements and  $^{13}\text{C}$  NMR relaxation measurements.

Although density and viscosity are the important fundamental properties characterizing liquid system, the reliable values of these physical properties of the

compounds have not been reported for proper working range. Hence the density and viscosity of these compounds were measured as a function of temperature in the range of -60 to +80°C.

The temperature dependence of the viscosity of Group 1 compounds is shown in Figure 14. The compounds with more side chains had higher viscosity, and this agreed with the general trend that a molecule of higher molecular weight has the greater viscosity than a low-molecular-weight compound with similar structure. From the observation that the temperature dependences of viscosity of three constitutional isomers (DEHP, DEHP, and DEHTP) are similar, the effect of the relative position of the substituents on the viscosity and viscosity index was not considered critical in this system.

It was interesting to compare the viscosity of compounds with aromatic benzene

#### The Effect of Conjugation on Viscosity

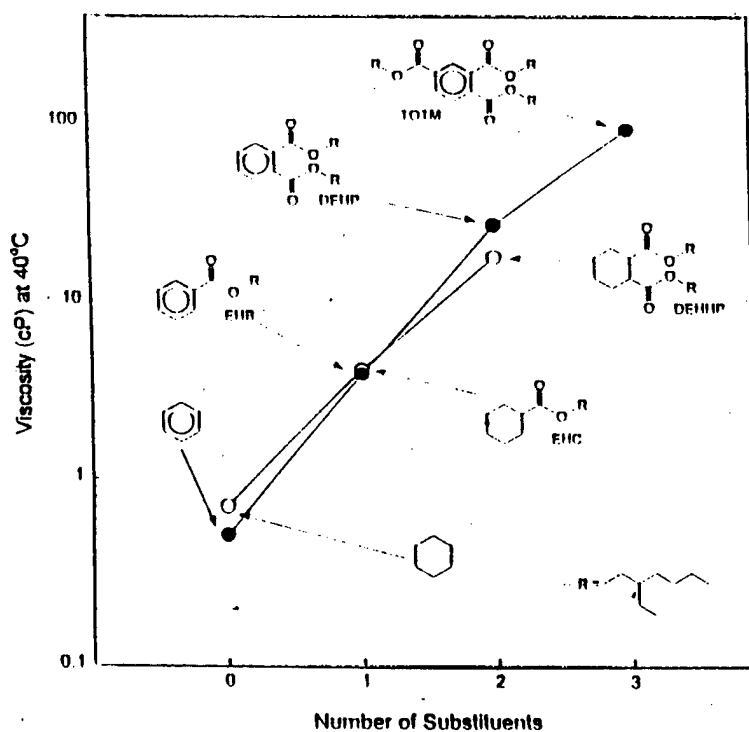


Figure 14

ring and with cyclohexane ring. Figure 14 shows the comparison between these two types of compounds. It is a general trend that the viscosity of the hydrocarbon fluid with cyclohexane ring is higher than that of the phenyl analog. However, the viscosity of the compounds with phenyl ring in Fig. 14 shows different behavior. It can be explained by the conjugation effect due to the delocalization of the electronic density around the conjugated double bonds. As the number of conjugated substituents increases, the increment of the viscosity is greater than the increment expected from the molecular weight increase. In the conjugated structure above, the hindrance of the molecular rotation about the C-C bond between the phenyl and the carbonyl group makes the molecule relatively rigid, which makes the liquid macroscopically more viscous.

#### VISCOSITY OF GROUP 2 COMPOUNDS

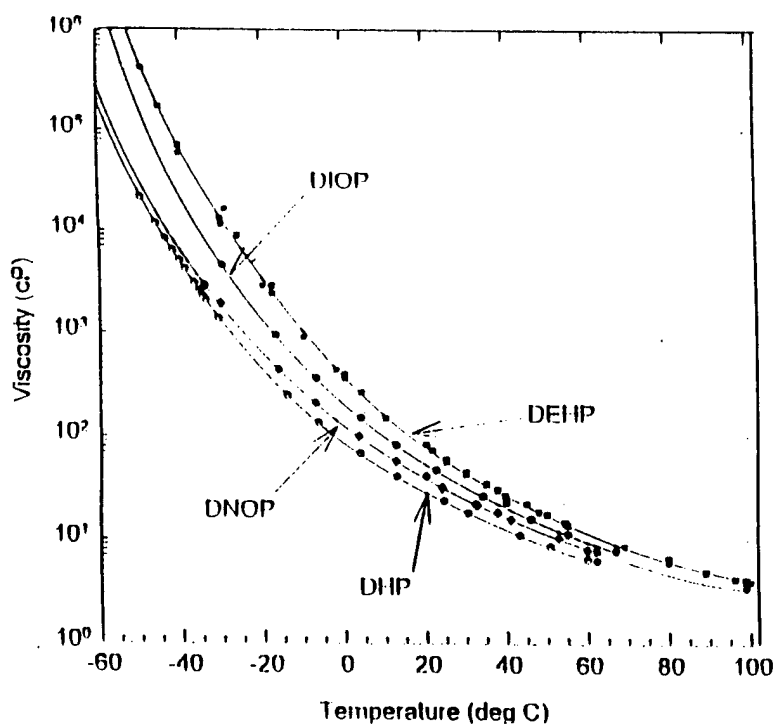


Figure 15

Figure 15 presents the temperature dependence of the viscosity of the molecules in Group 2 compounds. The comparison of the viscosity indicates that the presence of a branch in the side chain makes the fluid more viscous in phthalates. Also it seems to be more effective in increasing viscosity to have a branch near the rigid ring part of the molecules.

Natural abundance  $^{13}\text{C}$  NMR relaxation measurements provide excellent tool for the study of the molecular dynamics in fluids. The molecular level information on the motional behavior of the complex liquids can be obtained by measuring relaxation times and interpreting these relaxation data with a suitable theoretical model. We already tested several theoretical models and have known that the Cole-Davidson distribution model of the correlation times well explains the relaxation behavior of these complex liquids.

Carbon-13 spin-lattice relaxation time ( $T_1$ ) of these liquids were measured at 4.2 and/or 9.4 Tesla as a function of temperature. As a preliminary step of measuring the relaxation data, all of the individual  $^{13}\text{C}$  spectral peak were assigned using two-dimensional  $^1\text{H}$ - $^{13}\text{C}$  heteronuclear correlation (HETCOR) spectra. The relaxation data are analyzed in terms of a theoretical model assuming the Cole-Davidson distribution of the correlation times. In this model the parameter  $\beta$  represents distribution width and may assume a value from 0 to 1. As  $\beta$  approaches 0, the distribution becomes wider to the extreme case of the  $\beta=0$  limit, where infinite numbers of modes of motion are assumed. In the case of  $\beta=1$ , only one correlation time is present and it means that the motion of the specific nuclei is totally isotropic.

The comparison of  $\beta$  values of the selected compounds of Group 1 were shown in Figure 16. The fact that  $\beta$  values for 2-ethylhexyl ester side chain carbons are

very similar for all of the compounds indicates that the motional behavior of individual alkyl carbons in the side chain is not much affected by the structural change of the relatively rigid ring part of the molecules. Also it is shown that the presence of an additional chain makes the reorientation less anisotropic in DEHP and DEHHP than EHB and EHC, respectively.

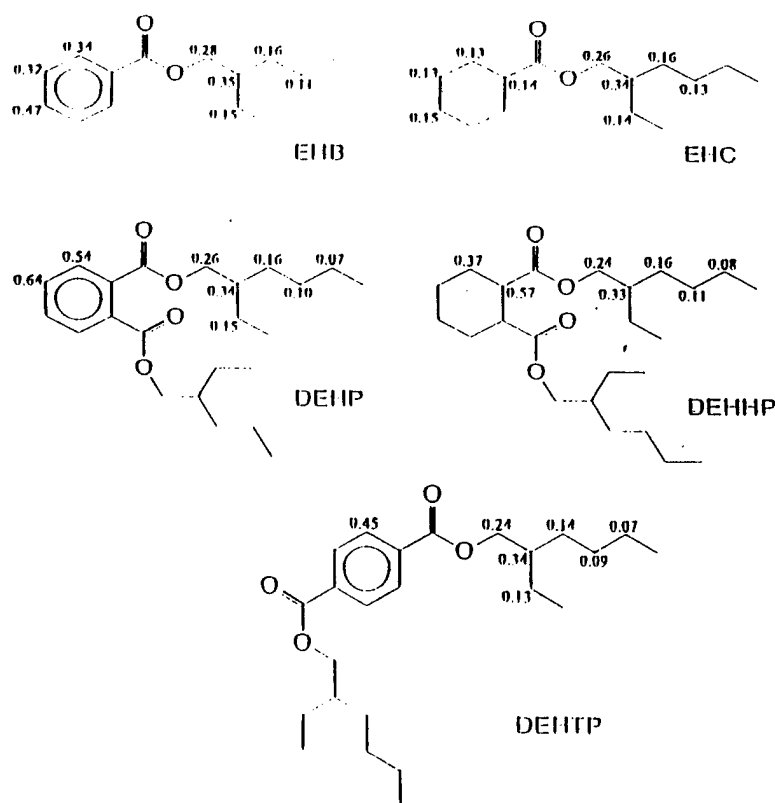


Figure 16

The  $\beta$  values of Group 2 compounds, which are compared in Figure 17, indicate that the motion of the carbon nuclei at the branching point is quite restricted. It is implied in this comparison that the flexibility of the branched side chain is greatly reduced, which explains the higher viscosity of the molecules with the branched ester side chains compared to the molecules with unbranched side chain.

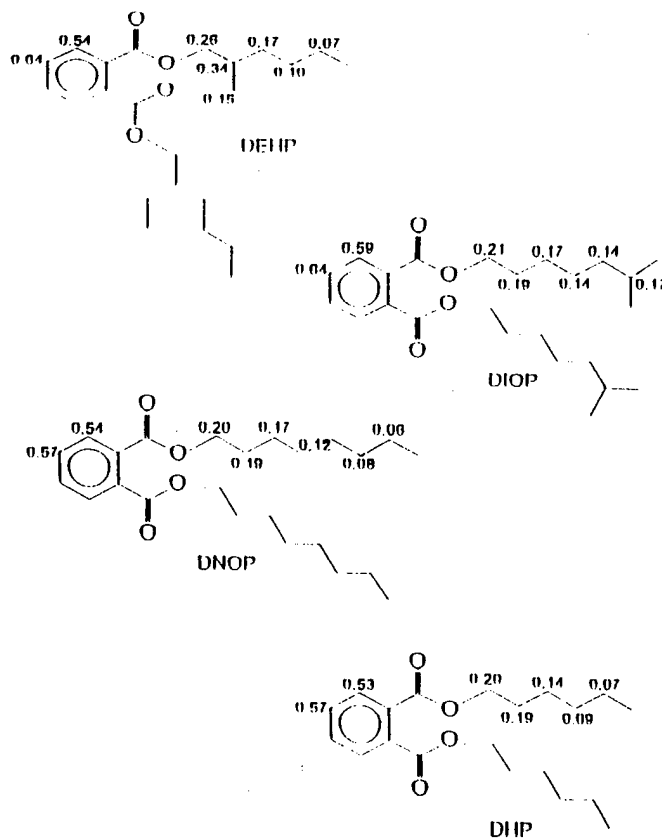


Figure 17

#### 1.4 SURFACE CRACK PROPAGATION UNDER COMBINED MECHANICAL AND HIGH PRESSURE FLUID LOADING

In this study, a mechanistic, self-consistent model has been developed using the fracture mechanics approach. The model can mainly be applied to ceramic materials in which inelastic deformation is limited during fracture. Microstructural features such as grain shape have been taken into account. Critical parameters which control the surface friction effect have been identified. The model predictions are compared with the experimental results of Suresh and Tschegg (*Journal of American Ceramic Society*, Vol. 70, 1987, p. 726-733) for a ceramic material under mixed mode I/mode III loading.

##### 1.411 Experimental Observations under Mixed Mode I/Mode III Loading

It has long been known that crack surface interaction such as surface rubbing and abrasion affects the fracture and fatigue crack growth behaviors under mode III (torsional) loadings. This effect was experimentally studied by Suresh and Tschegg in a brittle



material, 99.8%  $\text{Al}_2\text{O}_3$ . They used compression-compression cyclic loading to generate fatigue precracks of different lengths in notched bar specimens, and measured critical fracture loads for different combinations of tension and torsion. The precrack exhibits a typical intergranular fracture surface with the amplitude of surface roughness of the order of grain size. A fracture toughness locus in the  $K_I - K_{III}$  space (the locus of critical values of  $K_I$  and  $K_{III}$  at fracture) is obtained. Since there is little plastic dissipation during the fracture of ceramic material, an energy criterion for fracture should follow, i.e., the critical energy release rate,  $G_c$ , should be a material constant independent of the load mixity. For mixed mode loading, the energy release rate can be expressed in terms of the stress intensity factors, as

$$G = \frac{K_I^2}{E'} + \frac{K_{II}^2}{E'} + \frac{K_{III}^2}{2\mu}, \quad (5)$$

where  $E' = E$  ( $E$  is the Young's modulus) for plane stress configuration,  $E' = E / (1 - \nu^2)$  for plane strain configuration ( $\nu$  is the Poisson's ratio), and  $\mu$  is the shear modulus of the material. According to Equation (5) and the energy criterion for fracture, the critical stress intensity under pure mode III loading and that under pure mode I loading should obey the relationship,

$$K_{IIIc} = \sqrt{(1 - \nu)} K_{Ic}, \quad (6)$$

for a plane strain configuration. The value of  $K_{Ic}$  measured by Suresh and Tschegg was  $3.35 \text{ MPa}\sqrt{\text{m}}$ . The measured value of  $K_{IIIc}$ , however, was  $7.63 \text{ MPa}\sqrt{\text{m}}$ , 2.7 times the expected value from Equation (6).

In this research, we have developed a mechanistic model based on these experimental observations to quantify the surface friction effects.

#### 1.412 Governing Equations of a Crack with Surface Friction

As an idealized model, we consider an infinite body with a semi-infinite crack under far field mixed mode I/mode III loadings,  $K_I^{app}$  and  $K_{III}^{app}$ , as shown schematically in Figure 18. The total crack length is  $a$ . A portion of the crack face of length  $L$  experiences crack surface friction. Because of the friction, the crack tip stress intensities  $K_I^{tip}$  and  $K_{III}^{tip}$  should be modified from the far field applied stress intensities, as

$$\begin{cases} K_I^{tip} = K_I^{app} + K_I^{ind} \\ K_{III}^{tip} = K_{III}^{app} + K_{III}^{ind} \end{cases} \quad (7)$$

where  $K_I^{ind}$  and  $K_{III}^{ind}$ , are the induced stress intensities by the crack face friction.

The normal and shear frictional stress distributions along the surface  $L$  are denoted by  $\sigma_{f_I}(x)$  and  $\sigma_{f_{III}}(x)$ . The induced stress intensities can be obtained using the Green's function for stress intensities as

$$\begin{aligned} K_I^{ind} &= \int_L \sigma_{f_I}(s) G_{K_I}(s) ds \\ K_{III}^{ind} &= \int_L \sigma_{f_{III}}(s) G_{K_{III}}(s) ds \end{aligned} \quad (8)$$

where  $G_{K_I}(x)$  and  $G_{K_{III}}(x)$  are the Green's functions for stress intensities determined from the stress intensity for a pair of concentrated loads acting on the crack face at location  $x$ .

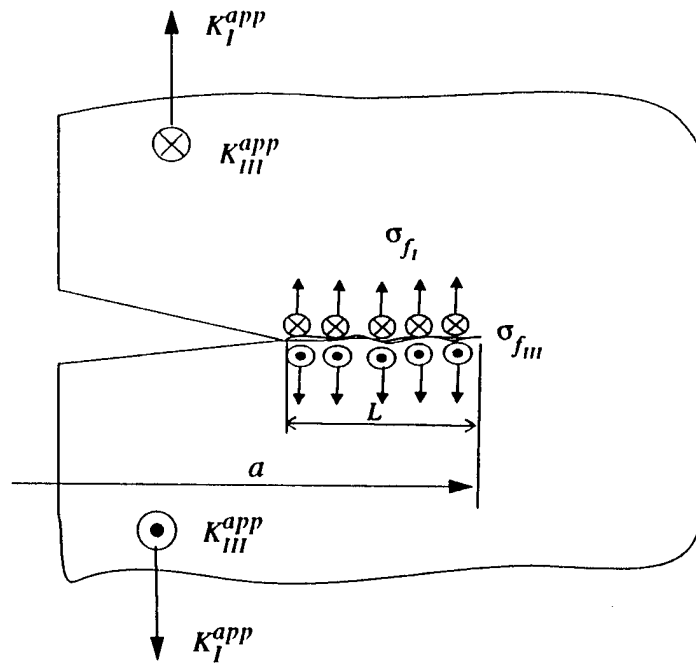


Figure 18. Schematic drawing of a cracked body with surface friction under mixed mode loading.

The fracture surface is assumed to be intergranular, with an average grain height of  $H$  and an average grain boundary oblique angle  $\alpha$  as shown in Figure 19. If we denote the relative crack opening displacement and out-of-plane shear displacement by  $v(x)$  and  $w(x)$ , respectively, the geometric considerations then require,

$$w \geq v \tan \alpha. \quad (9)$$

Without deformation of the grains, the equality in Equation (9) holds. It is noted that the opening

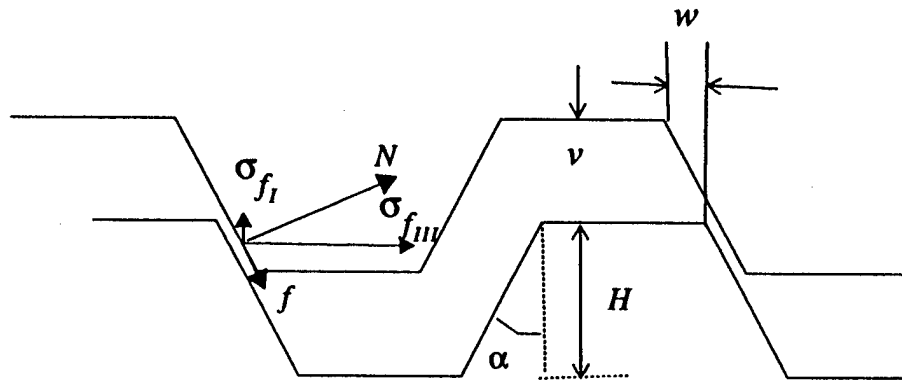


Figure 19. Crack surface morphology: geometry of interacting crack faces.

and shear displacements consist of two parts: one due to the applied far field stress intensities, one due to the surface frictional stresses. For linear elastic deformation of the cracked body, the total displacements can be obtained by the principle of superposition, as

$$\begin{aligned} v(x) &= v^{app}(x) + v^{ind}(x) \\ w(x) &= w^{app}(x) + w^{ind}(x) \end{aligned} \quad (10)$$

where  $v^{app}$  and  $w^{app}$  are displacements due to far field applied stress intensities, and  $v^{ind}$  and  $w^{ind}$  are due to surface frictional stresses. These displacement components can be expressed in terms of the far field applied stress intensities,  $K_I^{app}$  and  $K_{III}^{app}$ , and the Green's functions for the displacements,  $G_{U_I}(x, x')$  and  $G_{U_{III}}(x, x')$ .

To obtain the governing equation, we consider the relation between the normal compressive stress,  $N$ , and the frictional stress,  $f$ , on the grain boundaries as shown in Fig.

2. With some justification, a Coulomb type frictional law can be used here, i.e.

$$f = \mu_0 N, \quad (11)$$

where  $\mu_0$  is the friction coefficient of the sliding planes. The resulting mode I and mode III stress components can be related to the compressive and frictional stresses from equilibrium considering (Figure 2), as

$$\begin{aligned} \sigma_{f_I}(x) &= N \sin \alpha - f \cos \alpha = N(x)(\sin \alpha - \mu_0 \cos \alpha) \\ \sigma_{f_{III}}(x) &= N \cos \alpha - f \sin \alpha = N(x)(\cos \alpha - \mu_0 \sin \alpha) \end{aligned} \quad (8)$$

The self-consistency condition requires that the upper and lower crack faces are in contact, i.e., the equality in Equation (5) holds in the friction zone. This condition can be written in terms of frictional stresses, which gives rise to the governing equation, as

$$\begin{aligned}
& \sqrt{\frac{2}{\pi}} \frac{K_{III}^{app} \sqrt{x}}{\mu} - C_{III} \int \sigma_{f_{III}}(x') G_{U_{III}}(x, x') dx' \\
& = \tan \alpha \left[ \sqrt{\frac{2}{\pi}} \frac{K_I^{app} \sqrt{x}}{\mu} (1 - \nu) + C_I \int \sigma_{f_I}(x') G_{U_I}(x, x') dx' \right]
\end{aligned} \tag{13}$$

for  $x \in [0, L]$  where  $L$  is the length of the friction zone.

It is clear that this is an integral equation for the unknown frictional stress  $N(x)$ . Upon solving it, the frictional stress distributions as well as the crack tip stress intensities for given applied far field stress intensities can be obtained as functions of the geometrical parameter  $\alpha$  and the friction coefficient  $\mu_0$ .

#### 1.413 Solution Method

The governing equation, Equations (13), is an integral equation with singular kernels. A numerical method has been used to solve it. If we denote the normalized friction stress as  $\Sigma(s)$ , where the domain of interest is  $s \in [0, 1]$  ( $s = 1$  represents the end of the friction surface), Equation 13) can then be discretized by dividing the domain into  $n$  small intervals  $s_j$ ,  $j = 0, 1, \dots, n$ . The values of the unknown function at each point can be denoted by  $\Sigma_j = \Sigma(s_j)$ . The integrations can thus be evaluated with a weighted average approximation within each interval while treating the  $\Sigma_j$ 's as constants. The result of this operation yields a set of algebraic equations, as

$$K_{ij} \Sigma_j = g_i, \tag{14}$$

where  $K_{ij}$  is the coefficient matrix determined from the integration operation, and  $g_i$  is a vector obtained by evaluating from Equation (13). If the coefficient matrix can be inverted, the solution can be readily obtained by solving the algebraic equations. The

details of the solution method developed in this research can be found in Hsia, Zhang, and Socie (in *Fatigue and Fracture Mechanics: ASTM STP 1296*, pp152-174. 1977).

The above method of solution has proven to be an efficient way to solving the governing integral equation.  $n = 50 \sim 60$  was used to obtain the numerical solutions. A convergency test was performed for a range of  $n = 10 \sim 100$  which showed that  $n = 50$  is sufficient to obtain a convergent solution.

#### 1.414 Results - The Effective Stress Distribution $\Sigma(s)$

The spatial distributions of the non-dimensional effective stress  $\Sigma(s)$  were obtained for three different interaction zone combinations in Figure 20, where  $s = 0$  represents the crack tip, and  $s = 1$  is the point at the end of the friction zone. Figure 20 shows that for all three cases, pure frictional surface ( $L_y / L = 1.0$ ), pure smearing surface ( $L_y / L = 0.0$ ), and partial frictional and partial smearing surface ( $L_y / L = 0.5$ ), the effective stress does not approach zero at  $s = 0$  even though the relative displacement at the crack tip vanishes. This is due to the interlock between the upper and lower crack faces.

At the end of the friction zone ( $s = 1$ ), Fig. 20 shows that the pure friction model predicts that the effective stress approaches infinity, making it a singular point for the stresses. When the contacting surface consists of a friction zone and a smear zone, however, this singularity is removed. Figure 20 shows the effective stress distribution of two different cases: the pure smear zone case ( $L_y / L = 0.0$ ); and one half of the contacting surface is smear zone and the other half friction zone ( $L_y / L = 0.5$ ). In these

cases, the maximum value of the effective stress is finite and remains constant in the smear zone.

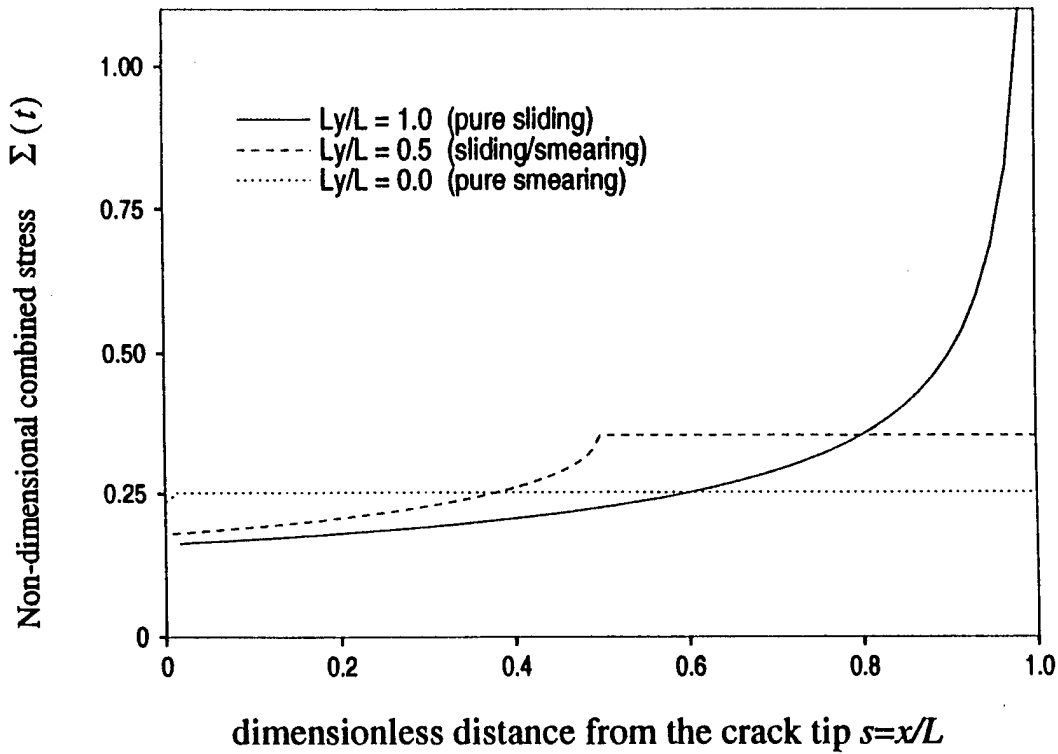


Figure 20. Non-dimensional effective stress distribution for various frictional surfaces.

### **Toughening Effect due to Surface Friction in Mixed Mode Fracture**

With the crack surface interaction, the crack tip stress intensities at fracture will be modified by the contributions from the frictional stress on the crack surface. The critical stress intensities will increase with the mode III stress intensity. This toughening effect can be characterized by plotting the critical energy release rate at fracture as a function of mode III applied stress intensity using the numerical solution.

The toughening behavior in terms of the fracture energy under mixed mode I/mode III loading can be easily seen in Fig. 21. The ratio of the applied energy release rate at fracture to the intrinsic critical energy release rate,  $G^{app} / G_c$ , is plotted as a function of

the applied mode III stress intensity in Figure 21. The figure shows that as the mode III component of the mixed mode loading increases, the apparent fracture energy increases rapidly. Moreover, the toughening effects become more profound as the friction coefficient increases or as the oblique angle decreases.

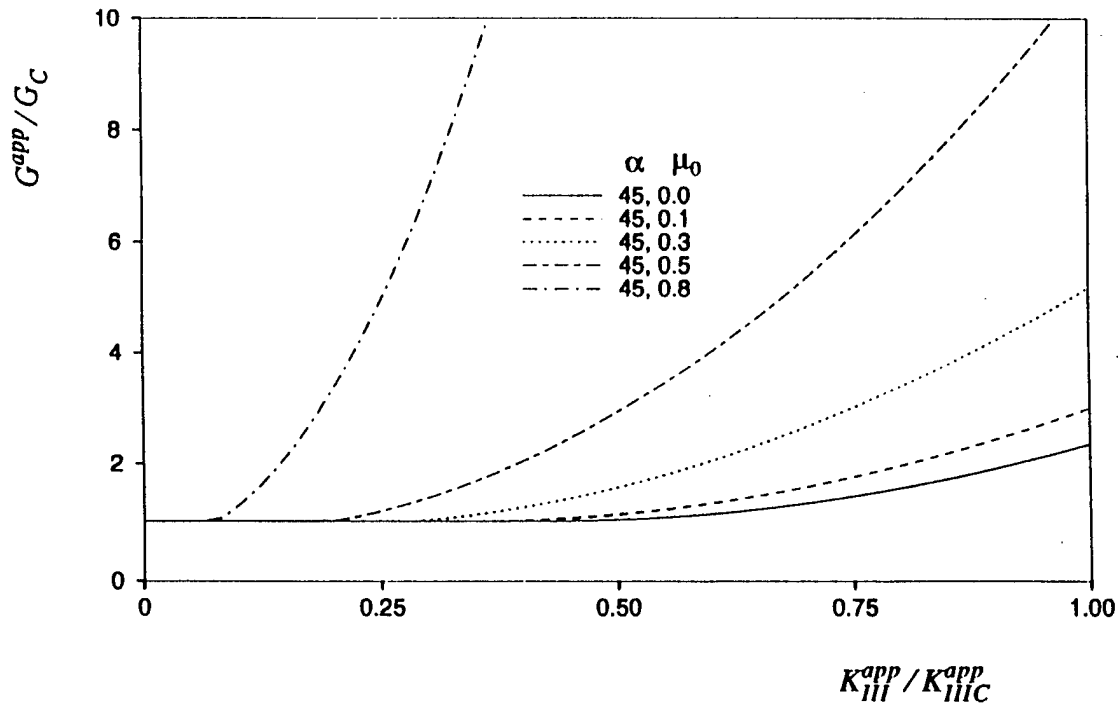


Fig. 21. The toughening ratio as a function of the relative magnitude of Mode III stress intensity.

#### 1.415 Comparison with Experiments

The predictions of the current model have been compared with the experimental results of Suresh and Tschegg. We selected a set of reasonable parameters which would best fit the experimental data. It was found that an oblique angle  $\alpha = 30^\circ$  and a friction coefficient  $\mu_0 = 0.1$  would yield a satisfactory result. Therefore, these values were used throughout the comparison.



Figure 22 shows the comparison of the predicted critical energy release rate at fracture and the experimental data as a function of the relative magnitude of the applied mode III stress intensity. For the selected parameters,  $\alpha = 30^\circ$  and  $\mu_0 = 0.1$ , excellent agreement is obtained between the model prediction and the experimental data.

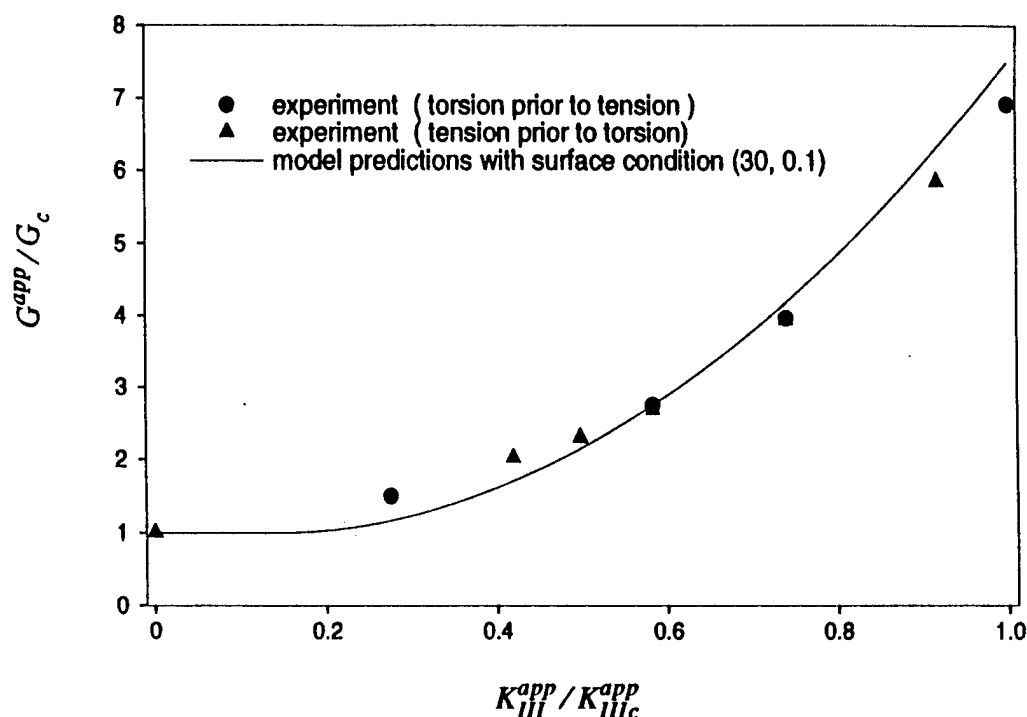


Figure 22. Comparison of model prediction and experimental measurements.

#### 1.416 Concluding Remarks

A mechanistic model has been developed to study the effects of crack surface friction on the fracture behavior of ceramic materials under general mixed mode I/mode III loading. This is the first time that microstructural parameters of materials have been taken into account in evaluating the behavior of a crack with surface friction. We have identified two important microstructural parameters which determine the toughening behavior due to crack surface friction: the grain boundary oblique angle  $\alpha$  and the grain

boundary friction coefficient  $\mu_0$ . The results of the present study show that the toughening effect due to crack face friction is independent of the grain size, but solely dependent on these two parameters. Furthermore, the study demonstrates that by introducing lubricating fluid, thus reducing friction on the crack surfaces, the toughening effects will be effectively reduced. Therefore a high crack propagation rate will result.

#### **1.42 Effects of High Pressure Fluid on Surface Crack Growth**

In rolling contact problems with lubricating fluid, the pressure build-up in the thin lubricant film between two contacting surfaces could be extremely high (on the order of Gpa). The high hydraulic pressure could substantially affect the surface crack initiation and surface crack growth behavior. In this project, we used fluid mechanics and fracture mechanics approaches to study the effects of hydraulic pressure on surface crack growth behavior.

Both experimental study and theoretical modeling have been pursued. The results from the experimental study and the modeling work are compared with each other and good qualitative agreement has been obtained.

##### **1.421 Theoretical Modeling**

We consider a crack filled with a linear viscous fluid in a semi-infinite body as shown in Fig. 6. The two different media involved in this problem are the viscous fluid and the cracked solid. The boundary conditions of the problem are such that the pressure history at the crack mouth,  $P_0(t)$ , is prescribed which is a periodic function of time; and the crack opening displacement at the crack tip,  $H(a,t)$ , is always zero. The initial pressure distribution in the crack can be arbitrary.

### Governing Equations

For the cracked body, assuming that the pressure distribution in the crack is  $p(x,t)$  and crack opening displacement is  $H(x,t)$ , they then obey an integral relations, as

$$H(x,t) = \int_0^a p(s,t) G(s,x) ds \quad (15)$$

where  $G(s,x)$  is the Green's function for the contribution of the pressure as  $s$  to the crack opening displacement at location  $x$ . On the other hand, fluid mechanics analysis leads to the following governing integral equation,

$$\frac{H^3}{12\mu} \frac{\partial p}{\partial x} + \frac{d}{dt} \int_x^a H(s,t) ds = 0 \quad (16)$$

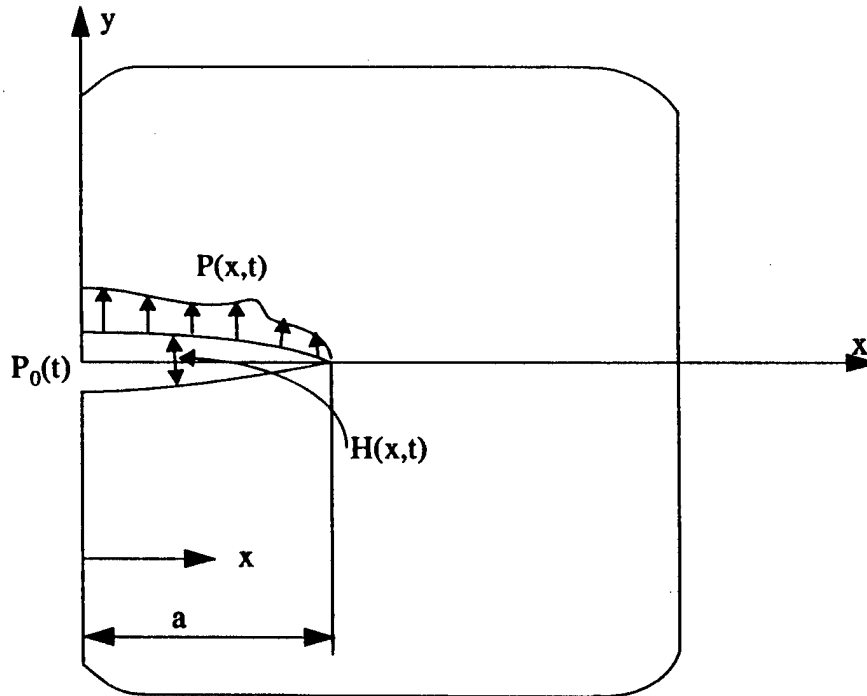


Fig. 23. An idealized model for a surface crack filled with viscous fluid.

for incompressible linear viscous fluid, where  $\mu$  is the viscosity of the fluid. The integral equation for the viscous fluid can also be re-derived to get a non-linear partial differential equation, as,

$$\frac{\partial H}{\partial t} = \frac{1}{12\mu} \frac{\partial}{\partial x} \left( H^3 \frac{\partial p}{\partial x} \right). \quad (17)$$

These two equations are coupled nonlinear integral-differential equations of two unknown functions, the fluid pressure distribution within the crack  $p(x,t)$  and the crack opening displacement profile  $H(x,t)$ . Solutions using two different approaches have been obtained: one approximate analytical solution by making assumptions about the relations between pressure distribution and crack opening displacement; and a numerical solution using finite difference method. The details of the solutions can be found in Hsia and Zu (*International Journal of Fracture*, **78**, 363-378, 1996) and Xu and Hsia (*ASME Journal of Tribology*, in press).

#### **An Approximate Analytical Solution**

To solve the two coupled integral equations analytically, an approximation was made. Instead of the global pressure versus opening displacement relation in (11), we assumed a local constitutive law similar to that used in analyzing beam on Winkler elastic foundations, i.e., the pressure at location  $x$  is assumed to relate only to the crack opening displacement at  $x$ . A nonlinear local constitutive law was used such as,

$$P(x,t) = C_\beta [H(x,t)]^\beta \quad (18)$$

where  $C_\beta$  is a proportionality coefficient, and the exponent  $\beta$  is a parameter which can be used to fit experimental data.

By making this approximation, the governing equations can be reduced to a non-linear differential equation as,

$$\dot{H} - K_\beta \frac{\partial}{\partial x} \left( H^{2+\beta} \frac{\partial H}{\partial x} \right) = 0 \quad (19)$$

where  $K_\beta = \beta C_\beta / 12\mu$ , and  $(\dot{\phantom{x}})$  denotes time derivative.

The method of separation of variables was used by decomposing  $H(x,t)$  into the product of two functions, one dependent on time only and the other on location only, as

$$H(x,t) = X(x)T(t). \quad (20)$$

Closed form solutions were obtained for the cases of  $\dot{H} > 0$ ,  $\dot{H} = 0$ , and  $\dot{H} < 0$ .

As an example, the time dependence of the crack opening displacement  $T(t)$  is plotted in Fig. 24 for the opening ( $\dot{T} > 0$ ) crack case. Fig. 24 shows that after the load is applied, there exists an incubation period before the crack opens up noticeably. But as the time approaches a characteristic time,  $\bar{t}_2$ , the amplitude of crack opening increases very rapidly. We call  $\bar{t}_2$  the *characteristic penetration time*, which is the time required for a pressure change at the crack mouth to be transmitted deep into the crack. The implication of this prediction of the model is that, if the pressure fluctuation at the crack mouth has a period much shorter than the characteristic penetration time, the crack tip will not feel the fluctuation; and vice versa. This conclusion has important consequences in rolling contact problems.

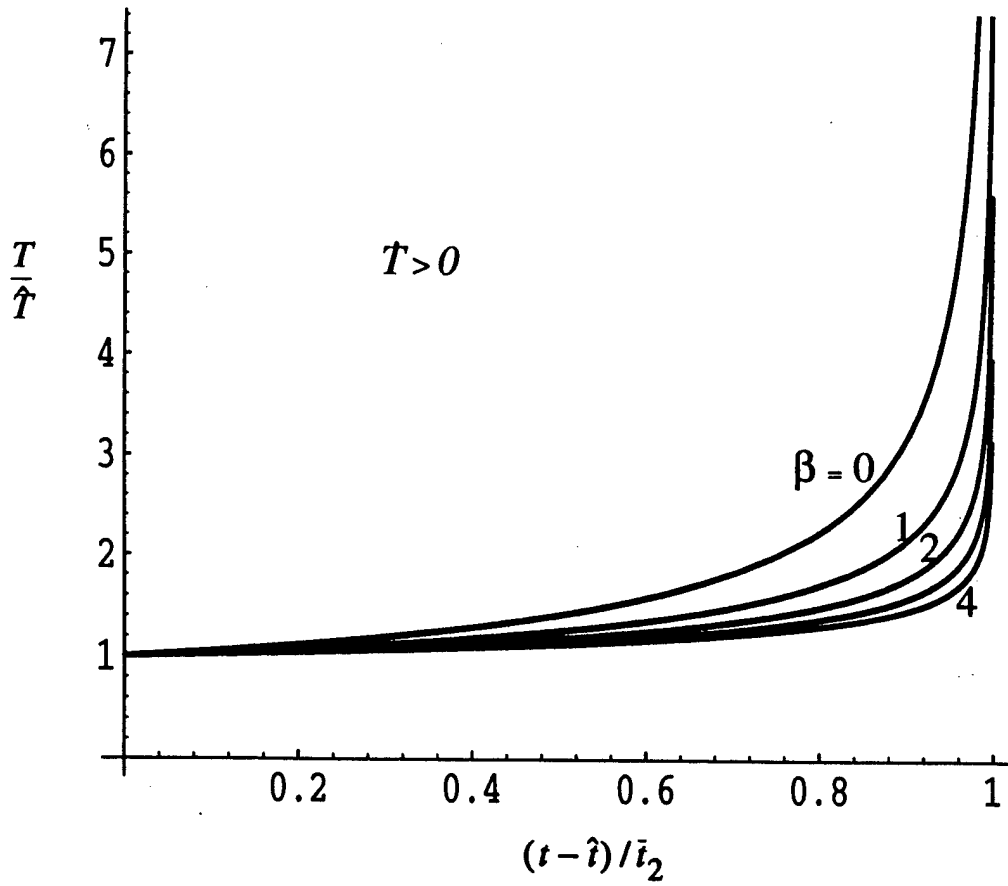


Fig. 24. Time dependence of the crack opening displacement.

The value of the characteristic penetration time is estimated by us as,

$$\bar{i}_2 = A_\beta \frac{\mu}{E'} \left( \frac{a}{\hat{H}} \right)^3, \quad (21)$$

where  $A_\beta$  is a dimensionless parameter of the order of unity, dependent on the exponent  $\beta$  and the boundary conditions. Equation (21) indicates that  $\bar{i}_2$  is proportional to the viscosity of the fluid, i.e., the more viscous the fluid is, the longer it takes for the pressure to be transmitted into the crack.  $\bar{i}_2$  is inversely proportional to the elastic modulus of the solid, so an elastically soft solid will make  $\bar{i}_2$  longer compared to an elastically stiff solid. Furthermore,  $\bar{i}_2$  is very sensitive to the slenderness ratio of the crack  $a/\hat{H}$ . A one order

of magnitude change in the value of  $a/\hat{H}$  results in three orders of magnitude change in the value of the characteristic penetration time.

### A Numerical Solution

The two coupled integral equations were also solved numerically using the finite difference method. The normalize domain of interest,  $\bar{x} \in [0,1]$ , was divided into  $N$  uniform intervals with the nodal coordinates  $\bar{x}_j (j = 0, 1, 2, \dots, N-1, N)$  and the corresponding nodal pressure values  $\bar{P}_j = \bar{p}(\bar{x}_j, \bar{t})$ . The  $N$  intervals were further groups into  $N/2$  sub-intervals,  $[\bar{x}_{m-1}, \bar{x}_{m+1}]$ , ( $m = 1, 3, 5, \dots, N-3, N-1$ ). The interpolation of the pressure distribution within each sub-interval was then given by,

$$\bar{p}_m(\bar{x}, \bar{t}) = \bar{p}(\bar{x}, \bar{t})|_{\bar{x} \in [\bar{x}_{m-1}, \bar{x}_{m+1}]} = A_m \bar{x}^2 + B_m \bar{x} + C_m, \quad (22)$$

where  $A_m, B_m, C_m$  were determined from the nodal pressure values,  $\bar{P}_{m-1}, \bar{P}_m, \bar{P}_{m+1}$ .

Time integration of the partial differential equation, Equation (17), was achieved using the finite difference method. For a given time increment,  $\Delta \bar{t}$ , the computational scheme is given by

$$\left[ \bar{H}_{i+1}^3 \left( \frac{\partial \bar{p}}{\partial \bar{x}} \right)_{i+1} - \bar{H}_{i-1}^3 \left( \frac{\partial \bar{p}}{\partial \bar{x}} \right)_{i-1} \right]^{(n+1)} = \frac{2}{N \Delta \bar{t}} \left( \bar{H}_i^{(n+1)} - \bar{H}_i^{(n)} \right), \quad (23)$$

here a fully implicit Euler time integration was used,  $\bar{H}_i^{(n)}$  denotes the opening displacement of note  $i$  at time step  $(n)$ . All other quantities in the equation were evaluated at time step  $(n+1)$ . Equation (23) represents a system of non-linear algebraic equations of the unknown vector,  $P = [\bar{P}_1, \bar{P}_2, \bar{P}_3, \dots, \bar{P}_{N-2}, \bar{P}_{N-1}]^T$ . In our calculation, constant time steps were taken.

At each time step, a Newton-Raphson iteration method was used to search the roots of the nonlinear algebraic equations. The solution was considered convergent when the absolute value of the error between subsequent step normalized by the value of the quantities themselves were lower than a prescribed tolerance.

Fig. 25 shows a typical transient solution of the pressure distribution at several different instants under a crack-mouth cyclic loading of sinusoidal wave (the insert above the plot). The time is measured in terms of the number of time steps  $n = \bar{t} / \Delta \bar{t}$ . It is clear from Fig. 25 that, upon applied cyclic loading at the crack mouth, the pressure is gradually transmitted into the crack. Eventually, the pressure at the crack tip may reach the same magnitude as the applied pressure at the crack mouth. This whole process represents the transient response of the fluid-solid system to external loading. The length of the transient

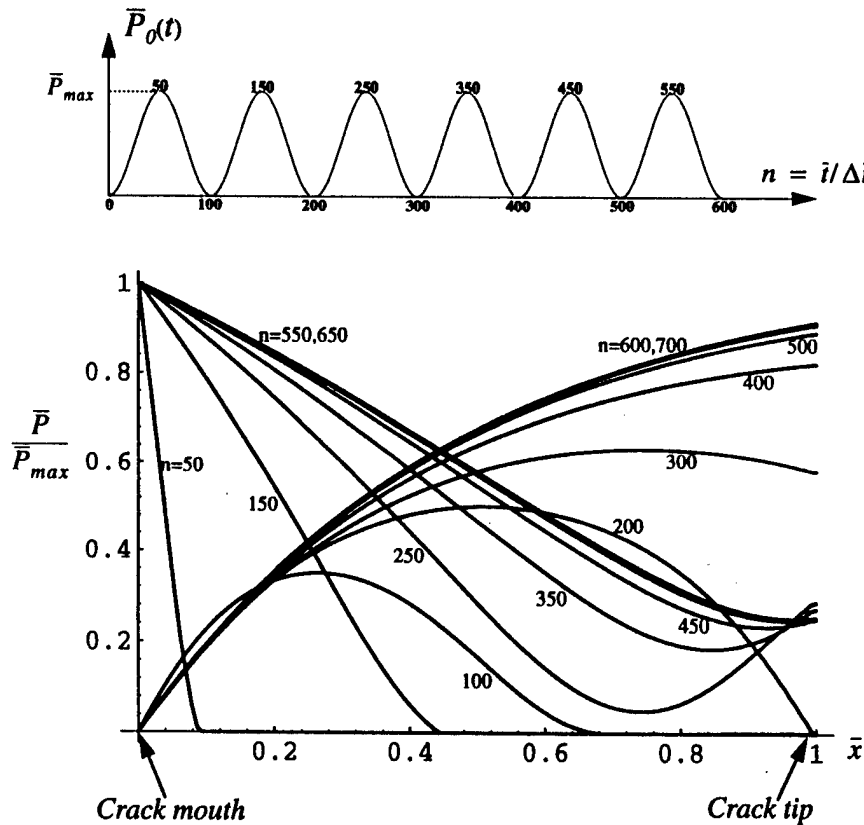


Fig. 25. Transient response of the pressure distribution with the crack.



stage depends on the viscosity of the fluid, the elastic property of the solid, and the loading frequency. The result indicates that, as predicted by the approximate solution by Hsia and Xu (*International Journal of Fracture*, 78, 363-378, 1966), there exists a characteristic penetration time for the fluid-solid system. When the length of the loading time is shorter than the characteristic time, the pressure change at the crack mouth can not be transmitted deep into the crack. On the other hand, if the length of loading time is longer than the characteristic time, a steady state pressure distribution is reached within the crack.

The steady state pressure distribution within the crack upon cyclic pressure loading of sinusoidal wave is shown in Figure 26. The pressure distribution in the crack repeats

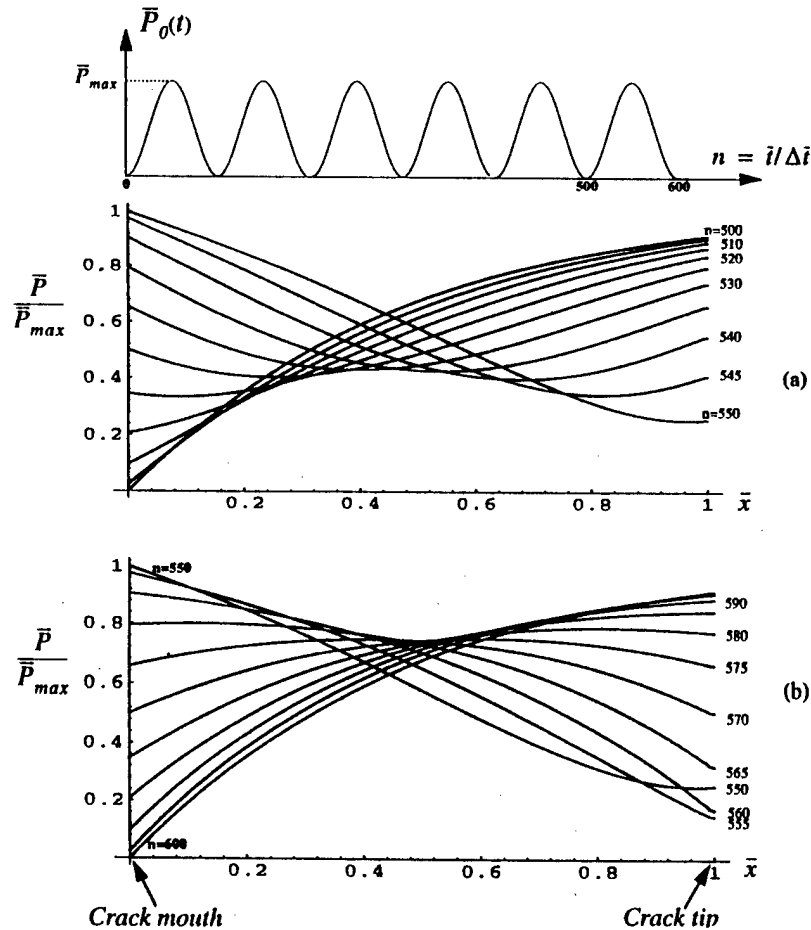


Figure 26. Steady state solution of the pressure distribution with a fluid filled crack.

itself completely upon each cycle of loading. The pressure build-up in the crack exhibits a phase shift from the applied pressure loading. When the applied pressure loading reaches the peak at  $n = \bar{t} / \Delta \bar{t} = 550$ , e.g., the pressure level deep in the crack is near its lowest level; whereas when the applied loading reaches the valley, the pressure deep in the crack is near its maximum level which is close to the peak level of the applied loading.

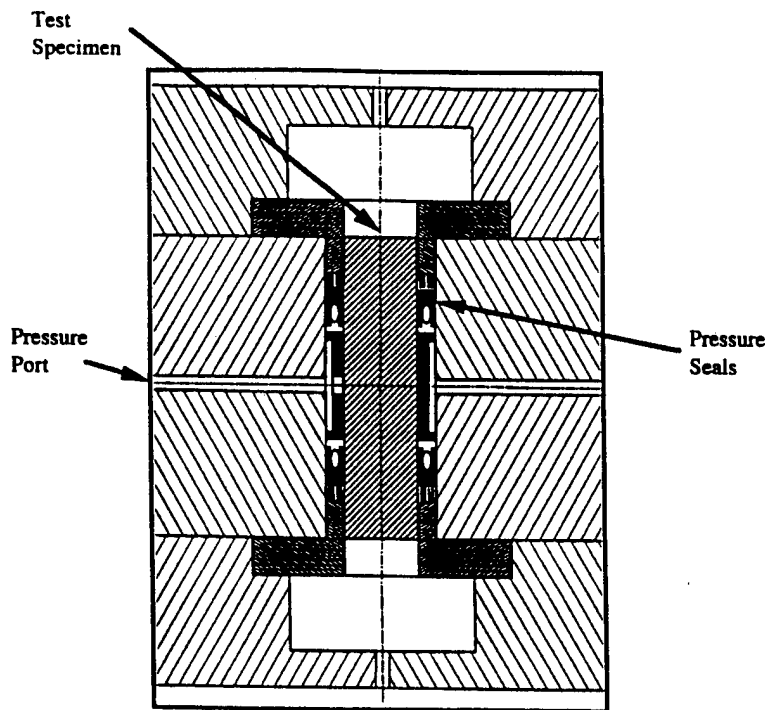
The results indicate that the present numerical method is very robust in studying the crack propagation behavior under hydraulic pressure loading. For material degradation due to surface crack propagation under rolling contact loading, the crack tip stress intensity factor can be easily evaluated for different types of loading using this model. The results obtained through the numerical simulations can also be readily compared with the experimental observations.

#### **1.422 Experimental Investigation**

##### Experimental Apparatus

Two different pressure loading systems were constructed. One system consisted of a pressure chamber connected to a pressure intensifier capable of supplying 20ksi (138 Mpa). The other, more complex system is capable of applying tension, torsion as well as pressure loading simultaneously.

The details of the pressure chamber of the first system is shown in Figure 27, in which the test specimen with surface cracks will be sitting on the testing table during the pressure loading. The chamber is equipped with two pressure ports to allow pressure measurements to be made in the pressure chamber to ensure greater accuracy. The tests were controlled by computer using LabView 3.0 and an AT-MIO-16x digital to analog



Expanded View, Pressure Test Apparatus

Figure 27. Details of the pressure chamber for pressure loading

converter board to receive data signal and send a driver signal to the test controller. A multi-state seal assembly was used to ensure a proper seal at pressures up to 20ksi. Each end of the test specimen was sealed with a Viton O-ring seal, a Teflon backup seal, and a brass backup ring with a steel seal spacer placed between the two sets of seals. The limiting factor in the operation is the frequency at which tests may be run. The hydraulic fluid does not immediately transmit pressure and therefore there is a lag time between pressurization of the intensifier chamber and the pressurization of the pressure chamber containing the specimen. The current system is capable of running fatigue tests at 0.5 Hz for the maximum 20ksi pressure amplitude.

The more complex system was built by modifying an MTS 930.73 multiaxial machine. The linear and rotary actuators of this machine as well as the load frame were used as the basis of a tension-torsion-pressure fatigue testing system. A Second linear actuator, an MTS 207.21-05 250kN actuator, was installed at the upper end of the load

frame such that three hydraulic actuators were available for the three testing modes (see Figure 28a). The testing system was controlled by a PC computer running LabView 3.0. load measurement was accomplished with an MTS/Lebow axial-torque load cell capable of measuring 100kip (445kN) linear load and 50 k lb- (5.65kN-m) torsional load. A simplified detail view of the pressure chamber surrounding the test specimen is seen in Figure 28b.

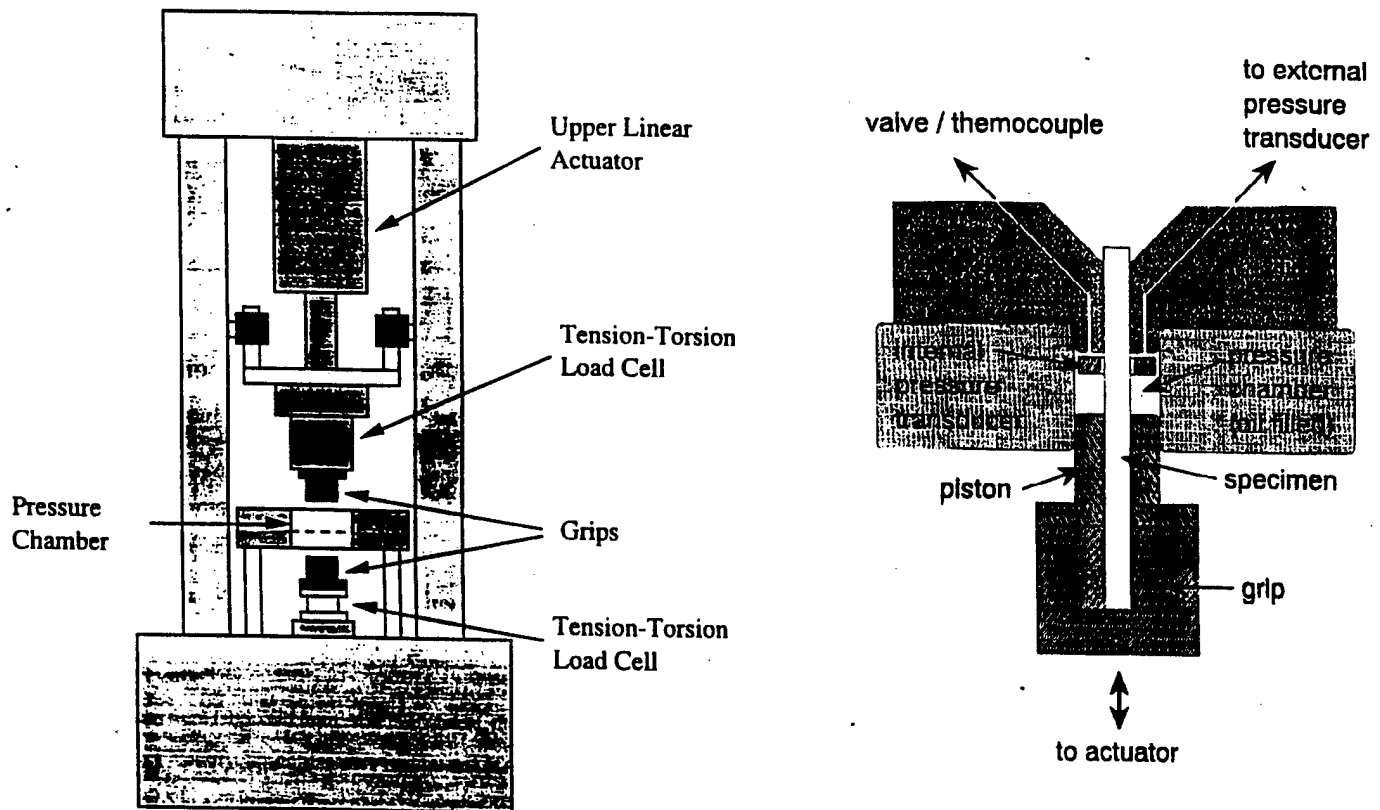


Fig. 28. Tension-torsion-pressure test apparatus: (a) load frame, (b) pressure chamber.

### Test Specimens

The AISI 52100 steel test material was received as 12.5 mm diameter round solid bars. Specimens 200 mm in length were cut from the bars followed by typical heat treatment in the roller bearing industry, SAE Aerospace Materials Specification 6440H.

Centerless grinding and polishing was performed after heat treatment to allow for easier optical monitoring of the fatigue crack length and reduce wear on the sliding high pressure seal in contact with the test specimen.

In order to control the location of crack initiation, a single small semi-spherical blind hole was drilled near the mid-point of each specimen using a YAG laser. Drilling parameters were adjusted to obtain holes with radii and depths of 140-290  $\mu\text{m}$ . Fatigue crack were initiated at the drill sites using a three-point bend apparatus followed by final precracking in axial tension. The pre-cracks were 350-100  $\mu\text{m}$  from the edges of the laser hole. The maximum axial stress for pre-cracking was less than the maximum hydraulic pressure used during the testing.

### **Testing Procedure**

Fluid of two different viscosities were used. The first was Mobile DTE-25 with a dynamic viscosity of  $\mu = 0.041 \text{ Pa} \cdot \text{s}$  at  $40^\circ\text{C}$ , and the second was Mobile SHC-634 with a dynamic viscosity of  $\mu = 0.41 \text{ Pa} \cdot \text{s}$  at  $40^\circ\text{C}$ . Pressure in the chamber was monitored by both an internal immersible pressure transducer surrounding the specimen and an external pressure transducer. Pressure measurements between the internal and the external transducers differed only when the higher viscosity oil was used in the chamber and the test frequency was greater than 2 Hz.

Cyclic hydraulic pressure loading was applied. All test were constant amplitude and run at a pressure ratio of  $R=0.05$  (minimum/maximum pressure). Test frequencies ranged from 3 to 0.017 hz ( $\sim 1$  cycle/minute). Higher frequency tests,  $f \geq 0.1 \text{ Hz}$ , was

conducted under a sinusoidal waveform while the lower frequency tests were under a trapezoidal waveform.

Surface crack length was monitored at regular intervals by removing the specimen from the test machine and examining the crack advance using a 100x-400x optical microscope with a calibrated eyepiece. Crack growth measurement resolution using this method is estimated to be approximately  $1\text{ }\mu\text{m}$ .

### Results

In order to compare the crack growth rate tested in pressurized oil, baseline data for the hardened 52100 steel was collected under uniaxial external loading in air. The results were analyzed using linear regression, and were shown in Fig. 29 as a solid line and dashed lines  $\pm 2$  standard deviation).

The test results of fatigue crack growth under hydraulic pressure loading in the less viscous oil are shown in Fig. 29. The results in the heavier oil are shown in Fig. 30. The regression curves are from the baseline data tested in air. A simple calculation using the

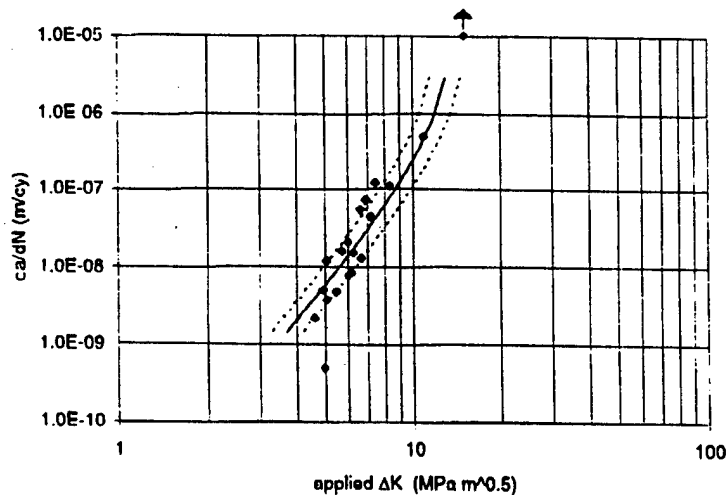


Figure 29. Measurement of fatigue crack growth rate under hydraulic pressure loading in light oil.

linear elastic fracture mechanics show that the external far field loading in air is equivalent to that of the pressurized fluid loading for fully penetrated fluid.

Fig. 29 shows that in light oil, the crack growth rate is the same as that under external loading in air for the frequency range considered in this study. This seems to indicate that in light oil, the fluid pressure applied in the pressure chamber can be fully transmitted deep into the crack. The pressure distribution within the crack is then nearly uniform. On the other hand, Fig. 30 shows that for tests in heavy oil, when the loading frequency is low, the crack growth behavior follows that under external far field loading. But when the loading frequency is high, the crack growth rate is significantly below the one under external loading or the crack does not grow at all. In Fig. 30, a dividing line between high and low frequency behavior based on the estimate of the characteristic penetration time obtained in Hsia and Xu's model is drawn. It is clear that the model predictions agree with the experimental measurements rather well.

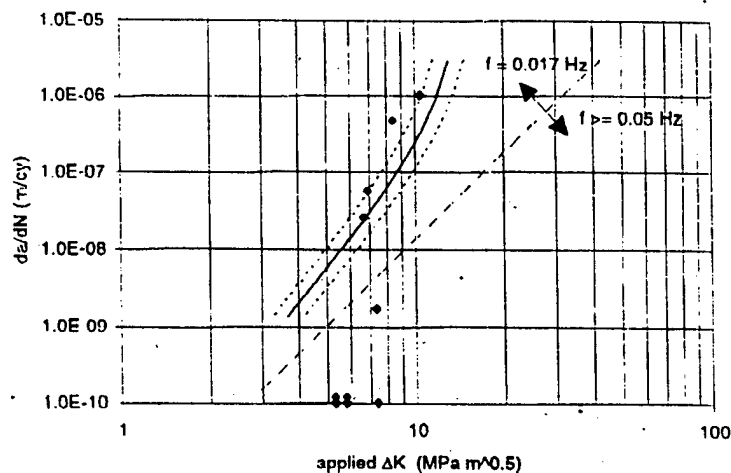


Fig. 30. Measurement of fatigue crack growth rate under hydraulic pressure loading in heavy oil.

## Conclusion

This sub-area of the AFOSR/URI on Material Degradation and Fatigue under Extreme Conditions has been focused on surface crack initiation and propagation under combined external loading and hydraulic pressure loading. Two thrusts have been actively pursued: the effects of crack surface friction on crack growth behavior, and the effects of high pressure fluid on surface crack growth. Both experimental investigation and theoretical modeling have been conducted.

A mechanistic model has been developed for the surface crack growth in the presence of crack surface friction under mixed mode I/III loading. The material toughening due to crack surface friction is studied. The model takes into account several microstructural and material parameters such as grain shape and friction coefficient between grain boundaries. By employing a self-consistent, fracture mechanics approach, the governing integral equation with a singular kernel is obtained. The numerical solution of the governing equation shows that, because of crack surface friction, the material toughens significantly. Moreover, two parameters, the oblique grain boundary angle and the friction coefficient, have been identified as the controlling parameters for the toughening behavior. The model predictions agree well with experimental measurements in a ceramic test.

The crack growth under combined external loading and hydraulic pressure have been studied through both experiments and theoretical modeling. The modeling effort focused on the interaction between pressurized viscous fluid and cracked solid. Using fluid mechanics and fracture mechanics method, the governing equations, two coupled integral equations of the fluid pressure distribution and the crack opening displacement,



were established. Both an approximate analytical solution and a numerical solution were obtained. The results identified a characteristic penetration time for the fluid-solid system. When the period of the cyclic pressure loading is shorter than the characteristic penetration time, the pressure fluctuations at the crack mouth will not transmit deep into the crack. Thus the crack growth rate is low. But when the period of the loading is longer than the characteristic time, full penetration of the viscous fluid is expected, resulting high crack growth rate. Full numerical simulations of the crack tip response under different hydraulic pressure loading at the crack mouth have been performed. An experimental apparatus has been constructed which is capable of applying external tension, torsion, and hydraulic pressure loading independently on rod-shaped specimens with surface cracks. Fatigue crack growth rates under both external loading and pressurized fluid loading in light and heavy lubricating oils have been measured. The results confirmed that whether the crack grows or not depends on whether the pressure can fully penetrate deep into the crack. While the crack growth behavior in a light oil is the same as that in air under external loading, the behavior in a heavy oil depends on the loading frequency. Low frequency pressure loading gives rise to full penetration of the pressurized fluid, resulting high crack growth rate. But high frequency loading may not result in any crack propagation at all, as predicted by the theoretical model.

The study represents the first attempt to model and experimentally investigate the complex fluid-solid system with a crack. Its success in predicting qualitatively the crack growth behavior under combined external and hydraulic pressure loading has important implications in material damage in rolling contact components in the Air Force applications. However, further studies are needed to address more realistic systems,

including the inclined surface cracks and change of fluid viscosity due to pressure change. These studies will provide guidelines for the material development engineers to come up with new materials and lubricants which will guarantee higher efficiency and safer operation of the next generation of aircraft.

## **1.5 Lubricant-Assisted Fatigue Crack Growth in Ceramics**

### **1.51 Repeated Indentation Method**

As an initial step in our investigation into the role of lubricants during failures of ceramic materials under the contact fatigue condition, repeated indentation studies were conducted to meet two primary objectives: a) developing a simple yet reliable method to determine if a lubricant would interact strongly with a ceramic material under the contact fatigue; b) understanding mechanical processes leading up to microfracture of ceramic surfaces under the contact fatigue.

The interaction between fluorinated lubricants (Krytox, Dupont) and a hot-isostatically-pressed silicon nitride (NT154, Norton) was examined by the repeated indentation method. This method required first indenting a polished ceramic surface in air at a predetermined load, covering the surface with a thin layer of a lubricant, and then repeating the indentation at the same area with the same indentation load for a number of times. On the  $\text{Si}_3\text{N}_4$  surface examined in our studies, indentation loads from 3 N to 30 N were applied to a Vickers indenter which indented the same area on the surface for up to 100 times. As shown in Figs. 31 and 32, the repeated indentation produced gradual chipping of the ceramic surface around the indentation. Following several indentations, a pit was formed around the indentation on the ceramic surface. As more indentations were

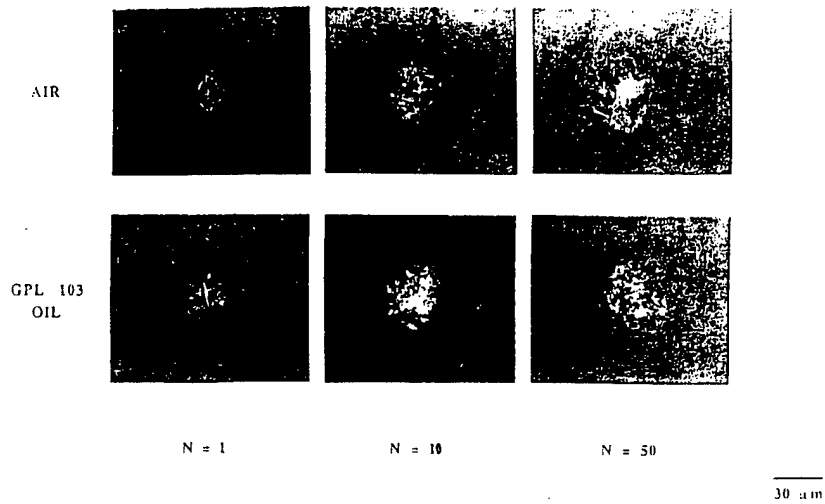


Fig. 31. Surface damage resulting from repeated indentations of  $\text{Si}_3\text{N}_4$  at indentation load of 3N.

repeated, the size of the pit grew and then reached a final size at which point the test was terminated.

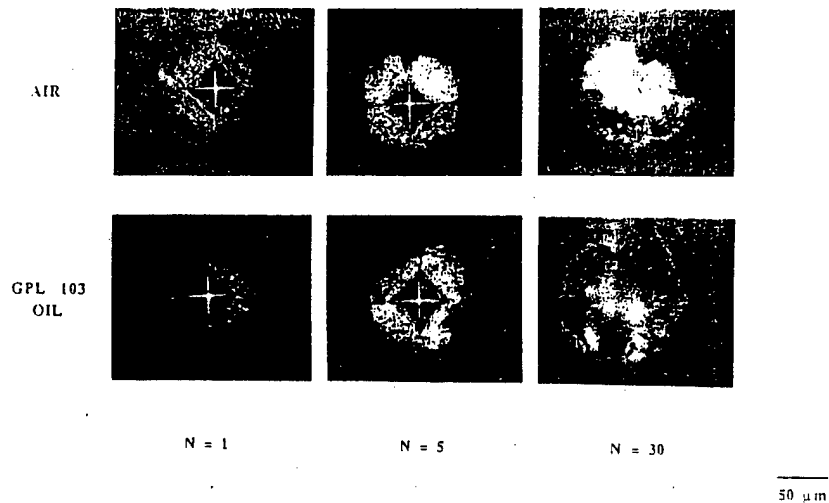


Fig. 32. Surface damage resulting from repeated indentations of  $\text{Si}_3\text{N}_4$  at indentation load of 30N.

The size of the surface damage was measured in terms of the total surface damage area (indentation plus the chipped area) after each indentation. The measurements were made for several different lubricants. At a given number of indentations, the ratio of the

damage size,  $D$ , vs. the initial indentation size,  $D_0$ , was computed for each lubricant and compared to that obtained in air to provide a quantitative indication how strongly a lubricant had interacted with the ceramic during the contact fatigue. As shown in Figs. 32 and 33, Krytox GPL 103 showed the most interaction with the silicon nitride. Therefore, subsequent surface-flaw studies were concentrated on this system.

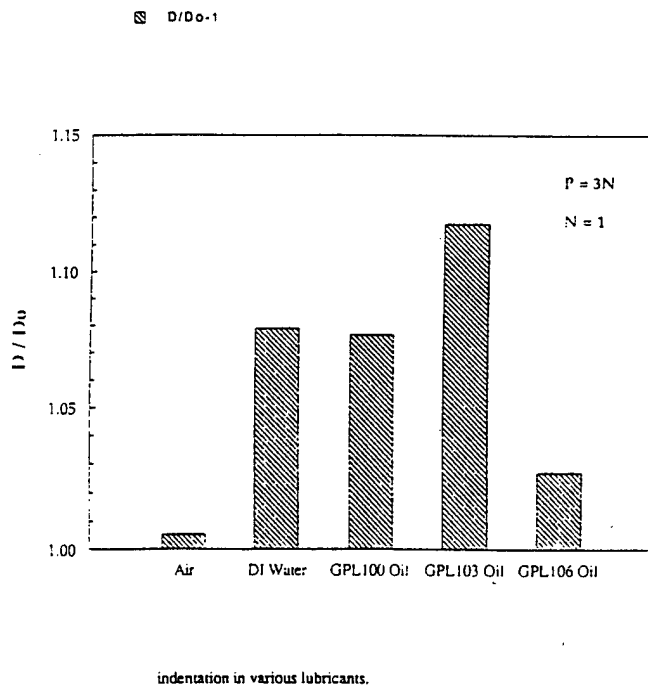


Fig. 33. Comparison of the surface damage sizes after one cycle of the repeated indentation in various lubricants.

In order to understand the mechanical processes leading up to surface chipping of a ceramic material under repeated indentation, we made a series of direct observations of the damage evolution under a Vickers indenter following repeated indentations of a single crystal aluminum oxide in air. The sapphire crystal was chosen because of its optical transparency, which allows direct optical imaging of flaws underneath the surface. The apparatus for the observation is shown in Fig. 34, which consists of an indentation stage driven by a micromotor, a Vickers indenter attached to a piezoelectric load cell, and an optical microscope. The indentation stage moves up and down to complete an indentation

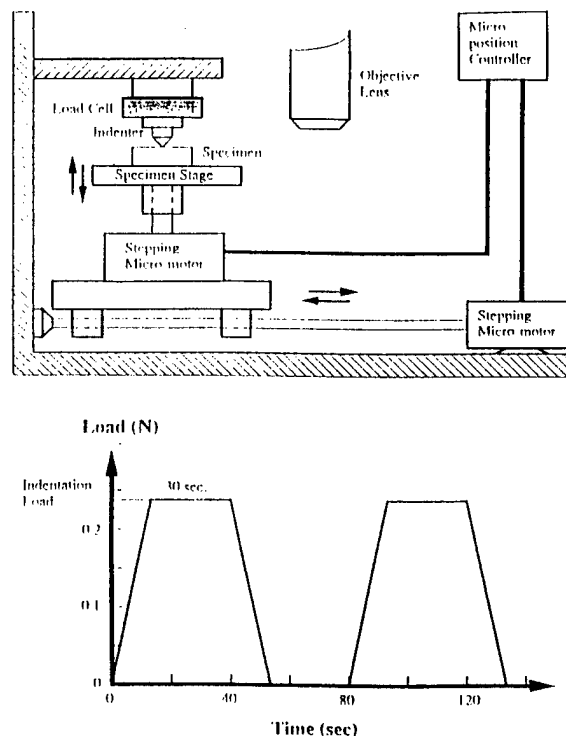


Fig. 34. Microindentation apparatus and load history.

cycle as shown in Fig. 34b, while the horizontal movement of the stage feeds the specimen to the microscope and to the indenter back and forth.

Our observations have shown that the damage evolution process under repeated indentations depends on the indentation load. As shown in Fig. 35, below a certain indentation load (about 0.5 N for sapphire), the damage began with a small impression on the surface. The surface impression expanded in area upon further indentation and tended to a triangular shape in accordance with the hexagonal symmetry of the crystal. After several repeated indentations, a small subsurface lateral crack emerged, which then grew laterally before turning upward to produce surface chipping. The number of indentations prior to the formation of the subsurface crack increased with decreasing indentation load. On a semi-log plot, the initiation time and the indentation load followed a straight line, similar to the fatigue S-N diagram known for metals.

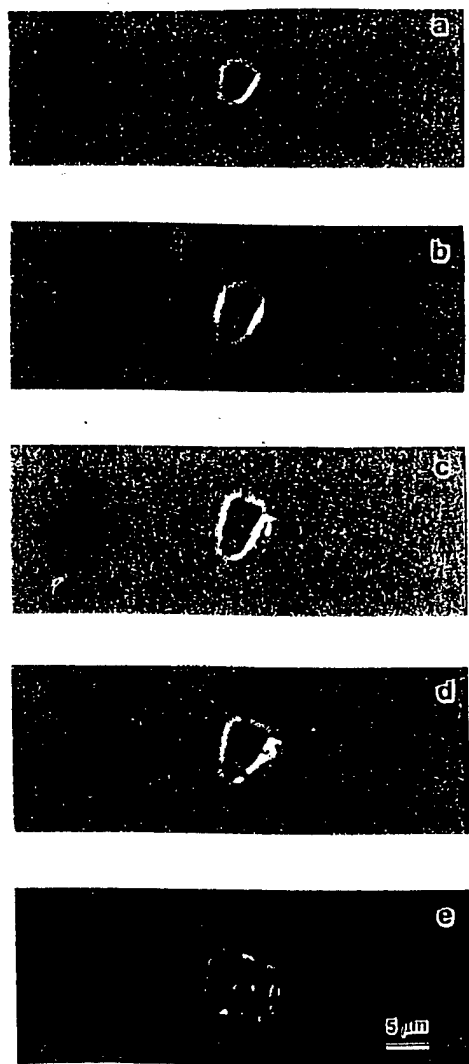
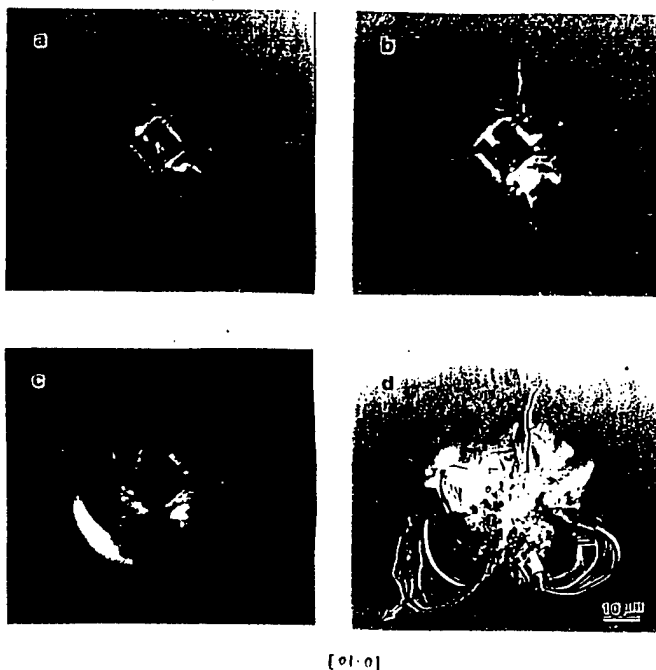


Fig. 35. Surface and subsurface damage at a low indentation load in sapphire.

(a)  $N = 1$ , (b)  $N = 2$ , (c)  $N = 5$ , (d)  $N = 10$ , (e)  $N = 20$ .

At higher indentation loads, lateral cracks appeared on the first indentation and then grew laterally. As seen in Fig. 36, they extended further out than those formed at lower indentation loads. Consequently, when these cracks turned upward, larger surface chips were produced. The growth of the subsurface crack under repeated indentations was analyzed by the indentation fracture mechanics. The crack growth rate per indentation,  $da/dN$ , is plotted against the stress intensity factor,  $K$ , in Fig. 37 for the lateral crack in the sapphire crystal.



(a)  $N = 1$ , (b)  $N = 5$ , (c)  $N = 10$ , (d)  $N = 15$ .

Fig. 36. Growth of lateral cracks at a high indentation load in sapphire.

### 1.52 Surface Crack Studies

In continuing our investigation into the role of lubricants during contact fatigue of ceramic materials, we conducted a series of fatigue studies on small surface flaws. Small surface flaws were interesting because a) they are close in size to microfractures of surfaces under contact fatigue, b) they provide a well-defined fracture mechanics condition, c) they have ready access to lubricants from the surface, and d) they can be directly imaged during fatigue experiments.

Growth of surface microcracks (50  $\mu\text{m}$  to 250  $\mu\text{m}$  in length) in a hot-isostatically-pressed silicon nitride was monitored by periodically measuring the crack length in four-point bend specimens subject to cyclic loading. Experiments were conducted in both air

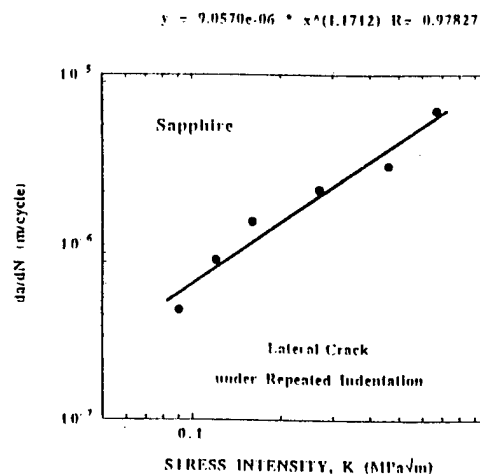


Fig. 37. Crack growth rate per indentation,  $da/dN$ , as a function of stress intensity for lateral cracks in sapphire.

and DuPont's Krytox fluorinated oil. For each testing environment, initial crack length and applied stress were systematically varied to obtain crack growth rates from  $10^{-11}$  to  $10^{-8}$  m/cycle. The growth behavior of microcracks in the oil and air is shown in Fig. 38 for one set of initial crack length ( $55\text{ }\mu\text{m}$ ) and applied stress (30/300 MPa). Cracks grew very rapidly for 15 to  $30\text{ }\mu\text{m}$  during the initial  $\sim 10,000$  cycles and then slowed down with progressively decreasing growth rates. The initial fast crack growth is believed to be a transient behavior associated with the change in the loading condition from monotonic overload (indentation) to cyclic fatigue. Following this transient period, cracks then entered into a period of slow growth, which lasted for over 50 pct of the lifetime, before they picked up the speed again to cause specimen fracture.

In the early portion of the crack-growth curve (first 30,000 cycles,  $\sim 4$  hr), no appreciable difference in crack growth between two environments was observed. However, clear difference was measured after specimens were tested in the oil for  $\sim 40,000$  cycles. As shown in Fig. 38, crack extension beyond 50,000 cycles was faster in the oil.

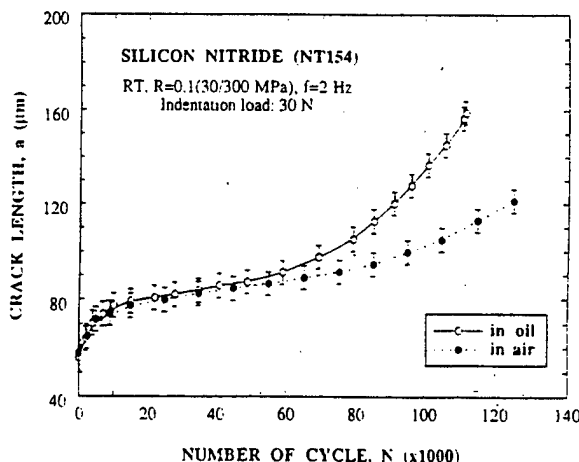


Fig. 38. Variation of crack length with stress cycles under fatigue loading of pre-indented specimens in the oil and air.

The same trend was observed for the specimens tested at different stress levels and the results are summarized in Fig. 39 in terms of the number of cycles to failure.



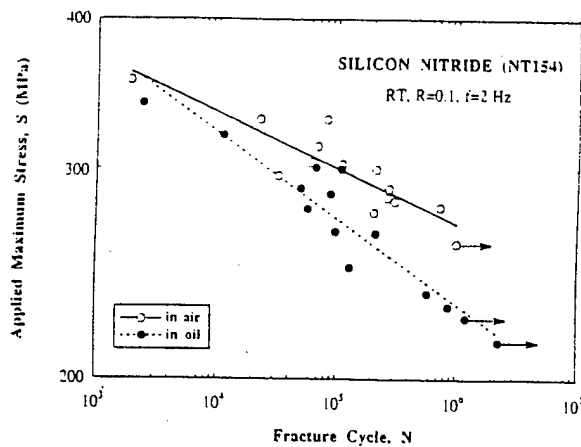


Fig. 39. Fatigue stress-life relation of pre-indented  $\text{Si}_3\text{N}_4$  specimen.

The effect of the lubricant on the growth of small surface flaws in  $\text{Si}_3\text{N}_4$  was further analyzed by the fracture mechanics. The results are plotted in Fig. 40 in terms of the fatigue crack growth per cycle,  $da/dN$ , as a function of stress intensity range,  $\Delta K$ . At the same  $\Delta K$ , the crack growth rate in the oil is seen to be at least twice as much as that in air. The accelerating effect of the oil was evident at all stress intensity ranges from the fatigue threshold to the fast fracture of the specimen.

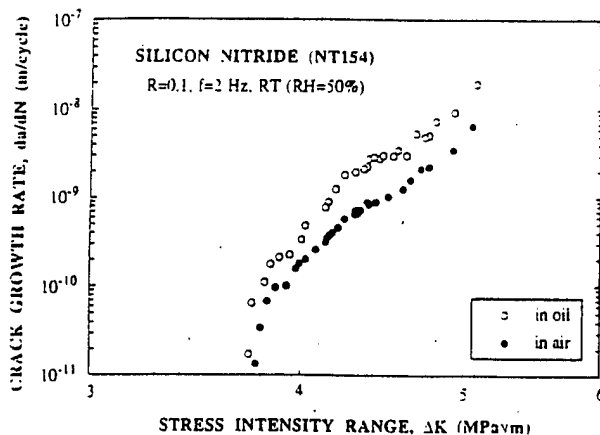


Fig. 40. Growth rates of surface cracks in air and in the fluorinated oil.

There were two plausible explanations to the effect of lubricating oil. One was the mechanics-based argument, which considered the oil-pressure build-up inside the crack as a mechanism to increase the crack tip stress. Another explanation was based on possible chemical interaction between the lubricant and  $\text{Si}_3\text{N}_4$ . To test which of the two arguments

was correct, we conducted fatigue experiments at elevated temperatures where the oil-pressure build-up inside the crack would be decreasing with increasing temperature and examined the chemistry of fatigue crack surfaces using XPS.

Crack growth in the Krytox 103 oil at three different testing temperatures is shown in Fig. 41. As the testing temperature was increased from 22° to 70°C, crack growth was

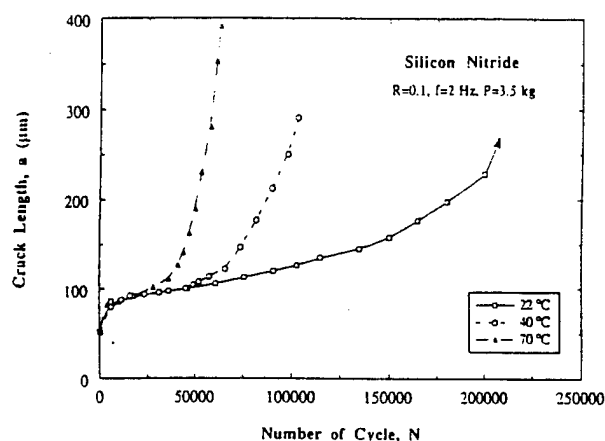


Fig. 41. Crack growth history in the fluorinated oil tested at three temperatures.

greatly accelerated. When analyzed in terms of the fracture mechanics, the fatigue crack rate is increased by roughly one order of magnitude for a fifty-degree increase in the oil temperature. If the variation of the fatigue crack growth rate with the oil temperature is fitted to a Boltzman-type equation of the form:

$$\frac{da}{dN} = A K^m \exp\left(-\frac{Q}{kT}\right)$$

where A and m are fitting constants. The activation energy, Q, was determined to be 40±5 kJ/mol. This is over five times as much as the activation energy for the viscous flow of the oil. Such a temperature-dependence is contrary to what to be expected from the argument based on oil-pressure build-up inside the crack and would be consistent with the stronger chemical interaction expected at higher temperatures.

Positive proof to support the explanation based on chemical reaction between the oil and  $\text{Si}_3\text{N}_4$  was obtained from XPS analysis of fatigue crack surfaces. The XPS spectra of the fatigue crack surface produced in the oil is given in Fig. 42. Upon analyzing the as-broken surface, two distinct F 1s peaks appeared (Fig. 42a). The peak on the left was identified to be the F-C peak whereas the one on the right, Y-O-F peak. Since the fatigue

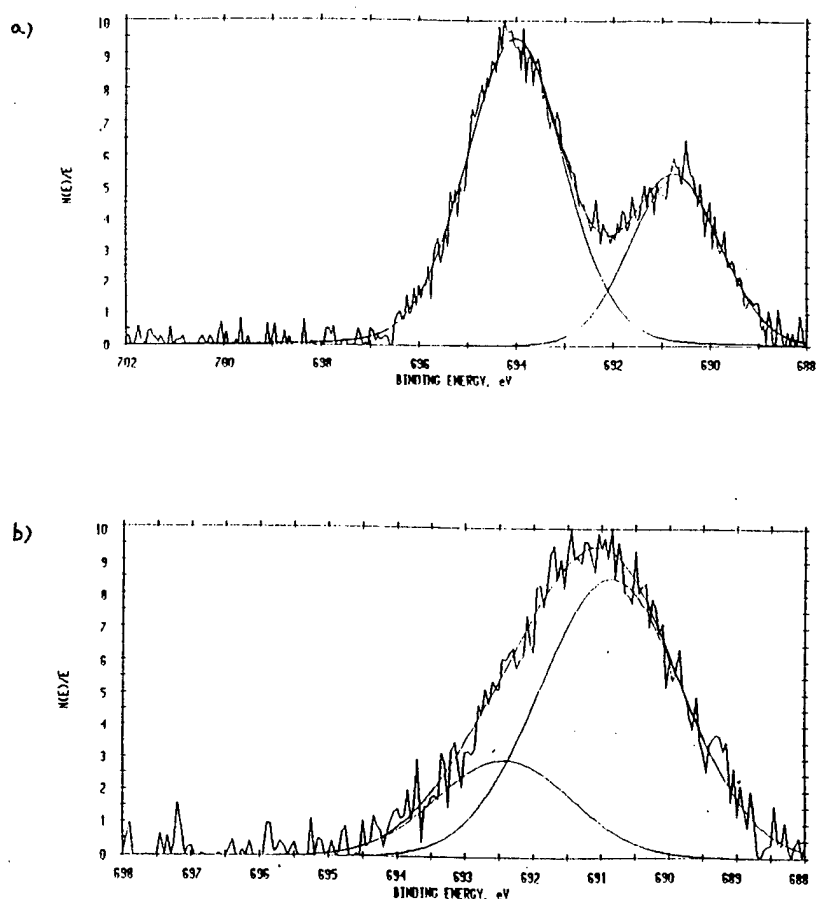


Fig. 42. XPS spectra of fatigue crack surface tested in oil: a) surface and b) after 5 min sputtering.

crack was developed in a fluorine-carbon oil and the  $\text{Si}_3\text{N}_4$  tested contained a grain boundary phase made up of mixed oxides of Y and Si, the F-C peak is considered to come from the oil, and the Y-O-F peak is related to the reaction product between the oil and the grain boundary phase. Following a 5 min sputtering of the broken surface, the oil residue was removed so that the F-C peak disappeared (Fig. 42b), but the Y-O-F peak remained.

As expected, in the fast fracture region of the broken surface, only the F-C peak was observed.

## 2.0 PUBLICATIONS ACKNOWLEDGING AFOSR SUPPORT

1. "The Investigation of Fluorinated Propenes on the Cu(111) Surface," J. M. Meyers, A.J. Gellman, *Surf. Sci.* 339, 57-67 (1995).
2. "Ultra-high Vacuum Boundary Lubrication of the Cu-Cu Interface by 2,2,2-Trifluoroethanol," C.F. McFadden, A.J. Gellman, *Langmuir* 11, 273-280 (1995).
3. "Effect of Surface Contamination on the UHV Tribological Behavior of the Cu(111)/Cu(111) Interface," C.F. McFadden, A.J. Gellman, *Trib. Lett.* 1, 201-210 (1995).
4. "FT-IRAS of Adsorbed Alkoxides: Ethoxides on Cu(111)," S.C. Street, A.J. Gellman, *Coll. and Surf. A* 105, 27-34 (1995).
5. "The Effect of Fluorine on the Bonding and Orientation of Perfluoroalkylethers on the Cu(111) Surface," J.M. Meyers, S.C. Street, S. Thompson, A.J. Gellman, *Langmuir* 12(6), 1511-1519 (1996).
6. "The Effect of Fluorination on the Surface Chemistry of Alkylethers on Cu(111)," J.M. Meyers, A.J. Gellman, *Trib. Lett.* 2, 47-54 (1996).
7. "Quantitative Adsorbate Orientation from Vibrational Spectra: Ethoxides on Cu(111)," S.C. Street, A.J. Gellman, *J. Chem. Phys.* 105, 7158 (1996).
8. "The Effect of Fluorination on the Bonding of Alkyl Ethers to the Al(110) Surface," J.M. Meyers, A.J. Gellman, *Surf. Sci.* 372, 171-178 (1997).
9. "Orientation of Physisorbed Propenes on Cu(111)," S.C. Street, A.J. Gellman, *J. Phys. Chem.* 101(8), 1389-1395 (1997).
10. "Fluoroether Bonding to Carbon Overcoats," L. Cornaglia, A.J. Gellman, *ASME/STLE Trans.*, ed. S. Bhatia (1996).
11. "FT-IRAS of Adsorbed Alkoxides: 1-Propoxide on Cu(111)," S.C. Street, A.J. Gellman, *Surf. Sci.* 372, 223-238 (1997).
12. "Metallic Friction: The Influence of Atomic Adsorbates at Submonolayer Coverages," C.F. McFadden, A.J. Gellman, in press *Surface Science*.

13. "The Surface Chemistry of Perfluorinated Ethers on Al<sub>2</sub>O<sub>3</sub> Thin Films," J.M. Meyers, R.M. Desrosiers, A.J. Gellman, submitted to *Trib. Lett.*
14. "Recent Progress in Ultrahigh Vacuum Tribometry," C.F. McFadden, A.J. Gellman, submitted to *Trib. Lett.*
15. "Fluoroether Binding to Carbon Overcoats," L. Cornaglia, A.J. Gellman, submitted to *J. of Vac. Sci. Tech.*
16. "The Interaction of Fluoroethers with Amorphous Hydrogenated Carbon," L. Cornaglia, A.J. Gellman, submitted to *Adv. Inf. Stor. Sys.*
17. "Transition States in Catalysis," M. Buelow, A.J. Gellman, submitted to *J. Mol. Cat.*
18. "Transition States for Reaction on Metal Surfaces," A.J. Gellman, submitted to *Langmuir*.
19. "The Effect of Molecular Adsorbates on Metallic Friction," C.F. McFadden, A.J. Gellman, in preparation.
20. "Surface Science Investigation of Fluorinated Hydrocarbons," C.F. McFadden, A.J. Gellman, review paper in preparation.
21. "Controlled Environment Measurements of Quasicrystal Friction," J.S. Ko, A.J. Gellman, in preparation.
22. "From Static to Kinetic Friction in Confined Liquid Films," G. Reiter, A. L. Demirel, and S. Granick, *Science* 263, 1741 (1994).
23. "Stick to Slip Transition and Adhesion of Lubrication Surfaces in Moving Contact," G. Reiter, A. L. Demirel, J. Peanasky, L. Cai, and S. Granick, *J. Chem. Phys.* 101, 2606 (1994).
24. "Soft Matter in a Tight Spot: Nanorheology of Confined Liquids and Block Copolymers," S. Granick, A. L. Demirel, L. Cai, J. Peanasky, *Israel J. of Chemistry* 35, 75 (1995).
25. "Nanorheology of Polymers, Block Copolymers, and Complex Liquids," A. L. Demirel, L. Cai, A. Dhinojwala, S. Granick, J. M. Drake, *MRS Proceedings* 366, 113 (1995).
26. "What Determines Static Friction?" G. Reiter, A. L. Demirel, J. Peanasky, L. Cai, S. Granick, *Tribology Lett.* 1, 1 (1995).

27. "Critique of the Friction Coefficient Concept for Wet (Lubricated) Sliding," A. Dhinojwala, L. Cai, and S. Granick, *Langmuir* 12, 4537 (1996).
28. "New Approaches to Measure Interfacial Rheology of Confined Fluids," A. Dhinojwala and S. Granick, *J. Chem. Soc. Faraday Trans. 4*, 619 (1996).
29. "The Solid-Like State of a Confined Liquid Lubricant," G. Reiter, A. L. Demirel, J. Peanasky, L. Cai, S. Granick, In B. Persson, Ed., *Physics of Sliding Friction*, NATO ASI Series, Kluwer Academic Publishers, Boston, 1996.
30. "What is Fluctuating in a Confined Liquid in the Stick-Slip Regime?" A. L. Demirel and S. Granick, In B. Persson, Ed., *Physics of Sliding Friction*, NATO ASI Series, Kluwer Academic Publishers, Boston, 1996.
31. "Glass-Like Transition of a Simple Fluid Confined Between Low-Energy, Noncrystalline Surfaces," L. Cai and S. Granick, In B. Bhushan, Ed., *Micro/Nanotribology and its Applications*, NATO ASI Series, Kluwer Academic Publishers, Boston, in press.
32. "Relaxations in Molecularly-Thin Liquid Films," A. Levent Demirel and S. Granick, *J. Phys. Condensed Matter* 47, 9537 (1996).
33. "Glass-Like Transition of a Confined Simple Fluid," A. Levent Demirel and S. Granick *Phys. Rev. Lett.* 77, 2261 (1996).
34. "Friction Fluctuations and Friction Memory," A. Levent Demirel and S. Granick, *Phys. Rev. Lett.* 77, 4330 (1996).
35. "Notes on the Interpretation of Nanorheology Experiments," A. Dhinojwala, L. Cai, and S. Granick, In M. Drake, S. Troian, R. Kopelman, Y. Klafter, Eds., *Dynamics in Small Confining Systems*, in press.
36. "Shear of Confined Perfluorinated Polyethers: Effect of Side-Branching," Y.-K. Cho and S. Granick, *Wear* 200, 346 (1996).
37. "Molecular Tribology of Lubricants and Additives," Y.-K. Cho, L. Cai, and S. Granick, *Tribology International*, in press.
38. "Generalized Effects in Confined Fluids: New Friction Map for Boundary Lubrication," G. Luengo, J. N. Israelachvili, A. Dhinojwala, and S. Granick, *Wear* 200, 328 (1996).
39. "Nanorheology of Polymers," L. Cai, J. Peanasky, S. Granick, *Trends in Polymer Science* 4, 47 (1996).

40. "Surface Forces in the Tapping Mode: Permeability and Hydrodynamic Thickness of Adsorbed Polymer Brushes," A. Dhinojwala and S. Granick, *Macromolecules* **30**, 1079 (1997).
41. "Modeling of Crack Surface Interaction in Mixed Mode Fracture," T. L. Zhang, M.S. Thesis, Department of Theoretical and Applied Mechanics, University of Illinois at Urbana-Champaign, Urbana, IL, 1994.
42. "Fatigue Crack Growth of Internally Pressurized Cracks," R. Bartsch, M.S. Thesis Department of Mechanical and Industrial Engineering, University of Illinois at Urbana-Champaign, Urbana, IL, 1995.
43. "Effect of Hydraulic Pressure on Surface Crack Propagation," J. Hsia and Z. Xu, in *Proc. International Symposium on Fracture and Strength of Solids*, FEFG '94, Xi'an, China, Ed. K.-C. Hwang and Y. Shen, pp. 604-608 (1995).
44. "The mathematical framework and an approximate solution of surface crack propagation under hydraulic pressure loading," K. J. Hsia and Z.-Q Xu, *International Journal of Fracture* **78**, 363-378 (1996).
45. "Effects of Crack Surface Morphology on the Fracture Behavior Under Mixed Mode Loading," K. J. Hsia, T. L. Zhang, and D. F. Socie, in *Fatigue and Fracture Mechanics: 27<sup>th</sup> Volume, ASTM Special Technical Publication 1296*, R. S. Piascik, J. C. Newman, and N. E. Dowling, Eds., pp. 152-174 (1997).
46. "A Numerical Solution of a Surface Crack Under Cyclic Hydraulic Pressure Loading," Z.-Q. Xu and K.J. Hsia, *ASME Journal of Tribology*, paper No. 96-trib-55, to be published.
47. "The Effect of Loading Frequency on Surface Crack Growth Under Fluid Pressure Loading," Z.-Q. Xu and K. J. Hsia, manuscript in preparation.
48. "Crack Propagation Under Cyclic Hydraulic Pressure Loading: Experimental Investigation," G. Marquis and D. F. Socie, submitted to *International Journal of Fatigue*.
49. "Modeling of Surface Crack Using Distributed Dislocation Method," V. Damljanovic and H. J. Hsia, manuscript in preparation.
50. "Fluid-Assisted Fatigue Crack Growth in Si<sub>3</sub>N<sub>4</sub>," D. Yao and J. K. Shang, *Cera. Engng. Sci. Proc.*, vol. 15, 1994, pp. 625-33.
51. "Lubricant-Enhanced Fatigue Crack Growth in Silicon Nitride," D. Yao and J. K. Shang, *Tribology Transaction*, vol. 38, pp. 973-79, 1995.

52. "Effect of Aging on Fatigue Crack Growth at Sn-Pb/Cu Interfaces," D. Yao and J. K. Shang, Metallurgical and Materials Transaction A, vol. 26A, pp. 2677-85, 1995.
53. "Effect of Cooling Rate on Interfacial Fatigue Crack Growth in Sn-Pb/Cu Joints," D. Yao and J. K. Shang, IEEE Transactions: CPMT, Vol. 19, No.1, 1996, pp. 154-165.
54. "An Experimental Technique for Studying Mixed-Mode Crack Growth in Solder Joints," D. Yao, Z. Zhang, and J. K. Shang, J. Electronic Packaging, Vol. 118, pp. 45-48, 1996.
55. "Effect of Load-Mix on Fatigue Crack Growth in Sn-Pb Solder Joints," D. Yao and J. K. Shang, ASME Paper 95-WA/EEP-10; J. Electronic Packaging, in press.
56. "Effect of Interface Roughness on Fatigue Crack Growth in Sn-Pb Solder Joints," D. Yao and J. K. Shang, J. Electronic Packaging, Vol. 118, pp. 170-173, 1996.
57. "Fatigue Crack Initiation in Solder Joints," Z. Zhang, D. Yao, and J. K. Shang, J. Electronic Packaging, Vol. 118, 41-44, 1996.
58. D. Yao, Ph.D. dissertation, University of Illinois, October 1995.
59. "Pressure as an Experimental Variable in NMR Studies of Molecular Dynamics," J. Jonas, Nuclear Magnetic Resonance Probes of Molecular Dynamics, Ed. R. Tycko, (Kluwer Academic Publ., NY), 1994, 265-299.
60. "NMR and High Pressure," J. Jonas, Encyclopedia of NMR, 1994, in press.
61. "High-Pressure NMR," J. Jonas, Contribution to the Encyclopedia of NMR, Ed. D. M. Grant and R. K. Harris, (J. W. Wiley, England), 1995, 2360-2370.
62. "Quenched Molecular Reorientation in Confinement," J.-P. Korb, L. Malier, F. Cros, Shu Xu, and J. Jonas, Materials Research Society Symposium on Dynamics in Small Confining Systems II 366, 265-270 (1995).
63. "Dynamic Structure of Methylcyclohexane and Perfluoromethylcyclohexane Liquids in Confinement and in Bulk," Shu Xu, L. Ballard, Y. J. Kim, and J. Jonas, J. Phys. Chem. 99, 5787-5792 (1995).
64. "High Pressure  $^{13}\text{C}$  NMR Study of the Motional Dynamics of Liquid Di(2-ethylhexyl) Phthalate," Y. J. Kim and J. Jonas, J. Phys. Chem. 99, 6777-6788 (1995).



65. "Raman Noncoincidence Effect of the Carbonyl Stretching Mode in Confined Polar Liquids," S. L. Wallen, L. Nikiel, and J. Jonas, *J. Raman Spectrosc.* 26, 1019-1022 (1995).
66. "<sup>13</sup>C NMR Relaxation Studies of Pyridine and Pentafluoropyridine Liquids Confined to Nanopores of Porous Silica Glasses," X. Shu and J. Jonas, *J. Phys. Chem.* 100, 16242-16246 (1996).
67. "NMR Study of Molecular Dynamics of Ethanol and 2,2,2-Trifluoroethanol Liquids Confined to Nanopores of Porous Silica Glasses," L. Ballard and J. Jonas, *Langmuir* 12, 2798-2801 (1996).
68. "High Pressure NMR," L. Ballard and J. Jonas, *Annual Reports on NMR Spectroscopy*, Vol. 33, Chap. 3, 115-150 (1997).
69. "Surface dynamics of liquids in nanopores," J.-P. Korb, F. Cros, S. Xu, and J. Jonas, *Phys. Rev. Lett.* 77, 2312-2315 (1996).
70. "High Resolution NMR Probe for Experiments at High Pressures," L. Ballard, C. Reiner, and J. Jonas, *J. Magn. Res.* 123, 81-86 (1996).
71. "Surface Rotational Dynamics of Liquids Confined in Nanopores," J.-P. Korb, L. Malier, F. Cros, S. Xu, and J. Jonas, in *Proceedings of Materials Research Society Symposium*, in press.
72. "Quenched Molecular Reorientation and Angular Momentum for Liquids Confined to Nanopores of Silica Glasses," J.-P. Korb, S. Xu, F. Cros, L. Malier, and J. Jonas, *J. Chem. Phys.*, 107, 4044-4050 (1997).
73. "High Pressure Raman Non-Coincidence Effect and Conformation of Alkyl Side Chain in Alkyl Benzoates," V. L. Slager, H.-C. Chang, Y. J. Kim, and J. Jonas, *J. Phys. Chem.*, submitted June 1997.
74. "Dynamics of Complex Phthalate Liquids I: Structural Effects of Molecular Framework," Y. J. Kim and J. Jonas, *J. Phys. Chem.*, submitted 1997.
75. "Dynamics of Complex Phthalate Liquids II: Structural Effects of Side Chains," Y. J. Kim and J. Jonas, *J. Phys. Chem.*, submitted 1997.
76. "Effect of Hydraulic Pressure on Surface Crack Propagation," K. J. Hsia and Z. Xu, in *Proc. International Symposium on Fracture and Strength of Solids, FEFG '94*, Xi'an, China, Ed. K.-C. Hwang and Y. Shen, pp. 604-608 (1995).

77. "The mathematical framework and an approximate solution of surface crack propagation under hydraulic pressure loading," K. J. Hsia and Z.-Q. Xu, submitted to *Int. J. Fract.*
78. "Effects of Hydraulic Pressure on Fracture: A Numerical Solution," Z.-Q. Xu, K. J. Hsia, manuscript in preparation.
79. "Effect of crack surface morphology on the fracture behavior under mixed mode loading," Hsia, K. J. , T.L. Zhang and D.F. Socie, ASTM 27<sup>th</sup> National Symposium on Fatigue and Fracture of Materials, in press.
80. "A numerical solution of a surface crack under cyclic hydraulic pressure loading," Xu, Z.Q. and K.J. Hsia, Journal of Tribology, in press.

### 3.0 LIST OF PERSONNEL

**PI: DR. ANDREW GELLMAN**

Dept. of Chemical Engineering  
Carnegie Mellon University  
Pittsburgh, PA 15213-3890  
PH: 412-268-3848  
FAX: 412-268-7139

**Associates:**

Dr. A. Paul	(Postdoc)
Mr. C. McFadden	(GS)
Mr. J. Meyers	(GS)
Mr. S. Street	(GS)

Collective address for associates:

Dept. of Chemical Engineering  
Rooms B202 and B207 Doherty Hall  
Carnegie Mellon University  
Pittsburgh, PA 15213-3890  
PH: 412-268-3892/412-268-5662  
FAX: 412-268-7139

**PI: DR. STEVE GRANICK**

Dept. of Materials Science & Engineering  
204 Ceramics, MC-232  
University of Illinois  
Urbana, IL 61801  
PH: 217-333-5720  
FAX: 217-244-2278

**Associates:**

Y. K. Cho  
Dr. A. Dhinojwala (Postdoc)  
Dr. E. Enriquez (Postdoc)  
Mr. A. L. Demirel  
S. Sukhisvili  
Dept. of Materials Science & Engineering  
489 MRL, MC-230  
University of Illinois  
Urbana, IL 61801  
PH: 217-244-4423/217-333-3157\*

**PI: DR. K. JIMMY HSIA**

Dept. of Theoretical & Applied Mechanics  
216 Talbot Lab/225b Talbot Lab, \* MC-262  
University of Illinois  
Urbana, IL 61801  
PH: 217-333-2321/244-0566\*  
FAX: 217-244-5707

**Associates:**

T.-L. Zhang (GS)  
Dept. of Theoretical & Applied Mechanics  
225d Talbot Lab, MC-262  
University of Illinois  
Urbana, IL 61801  
PH: 217-333-4930

**PI: DR. JIRI JONAS**

Dept. of Chemistry  
166 RAL, MC-712  
University of Illinois  
Urbana, IL 61801  
PH: 217-333-2572  
FAX: 217-244-3993

**Associates:**

S. Xu (Postdoc)  
L. Ballard (Postdoc)  
Y. J. Kim (Postdoc)  
V. Slager (GS)

Collective address for associates:

Dept. of Chemistry  
Rooms 173-177 RAL, MC-712  
University of Illinois  
Urbana, IL 61801

PH: 217-333-3897 (RAL)\*  
217-333-3581 (MRL)\*  
217-333-7145 (MRL)\*  
FAX: 217-244-3993

**PI: DR. JIAN-KU SHANG**

Dept. of Materials Science & Engineering  
307 Met & Min, MC 246  
University of Illinois  
Urbana, IL 61801  
PH: 217-333-9268  
FAX: 217-333-2736

**Associates:**

D. Yao (GS)  
D. Zhu (Postdoc)  
Dept. of Materials Science & Engineering  
205b Talbot Lab, MC-262  
University of Illinois  
Urbana, IL 61801  
PH: 217-333-1052  
FAX: 217-333-2736

**PI: DR. DARRELL SOCIE**

Dept. of Mechanical & Industrial Engineering  
332D MEB, MC-244  
University of Illinois  
Urbana, IL 61801  
PH: 217-333-7630  
FAX: 217-244-6534

**Associates:**

E. R. Bartsch (GS)  
Z. Zu (Postdoc)  
G. Marquis (Postdoc)  
V. Damjanovic (GS)  
\*Designates lab address and/or phone.

**4.0 INTERACTIONS/TRANSACTIONS**

**4.1 Participation/Presentations**

A. J. Gellman:

**Conferences / Seminars**

American Chemical Society Meeting, Spring '93

- A. J. Gellman

American Physical Society Meeting, Spring '93	- A. J. Gellman
AVS/STLE Local Section Meeting, Spring '93	- A. J. Gellman
American Vacuum Society Meeting, Fall '95	- C.F. Mcfadden - S.C. Street
Fed. of Anal. and Applied Chemists Meeting, Fall '95	- S.C. Street
American Chemical Society Meeting, Spring '96	- A.J. Gellman
NATO ASI on Nanotribology, Summer '96	- Jeff Ko
New Horizons in Quasi-Crystal Research, Fall '96	- A.J. Gellman
American Physical Society Meeting, Spring '97	- A.J. Gellman
American Chemical Society Meeting, Spring '97	- A.J. Gellman
American Inst. of Chemical Eng. Meeting, Fall '97	- Jeff Ko

Visits to Universities / Companies to Talk about AFOSR Sponsored Work

Ethyl Petroleum Additives Inc., St. Louis, MO - Nov., 1993  
 Carnegie Mellon Univ., Data Storage Systems Ctr., Pittsburgh, PA - April, 1994  
 Aluminum Corporation of America, Pittsburgh, PA - Aug. 1995  
 Iowa State University, Dept. of Chemistry, Ames, Iowa - Sept. 1995  
 Carnegie Mellon Univ., Dept. of Mech. Eng., Pittsburgh, PA - Oct. 1995  
 Oxford University, Dept. of Materials Science, Oxford, U.K. - June, 1996  
 ETH - Zurich, Dept. of Materials, Zurich, Switzerland - June, 1996  
 Ohio University, Dept. of Physics, Athens, OH - Dec. 1996

S. Granick:

**Invited Lectures Concerning this Research**

**1993**

Exxon Research & Engineering, Annandale, NJ, 1/5  
 Purdue Univ., Dept. of Chemistry, West Lafayette, IN, 2/10  
 Lehigh Univ., Distinguished Polymer Lecture, Bethlehem, PA, 2/24  
 Exxon Research, Baytown, TX, 3/5  
 APS Symp. on Surface Chemistry, Seattle, WA, 3/22  
 ACS Symp. on Tribology, Denver, CO, 3/28  
 Univ. of Minnesota, Dept. of Chemistry, Minneapolis, MN, 4/9

Stanford Univ., Dept. of Chemical Eng., Stanford, CA, 5/19  
Intl. Mtg. on Relaxations in Complex Systems, Spain, 6/28  
Gordon Conf. on Chemistry and Physics of Liquids, N.H., 8/9  
ACS Symp. on Adhesion, Chicago, IL, 8/23  
Intl. Mtg. on Adsorbed Polymers, Bristol, U.K., 9/5  
Univ. of Delaware, Dept. of Chem. Eng., 10/1  
Iowa State Univ., Dept. of Chemistry, 10/22  
Rhône-Poulenc Intl. Symp. on Interfaces, Paris, France, 11/24  
Hong Kong Polytechnic Univ., Hong Kong, 12/21

#### 1994

Kyoto Univ., Dept. of Polymer Chemistry, Japan, 1/21  
Kyoto Univ., Dept. of Polymer Chemistry, Japan, 1/28  
Nagoya Univ., Dept. of Physics, Japan, 2/23  
Kyoto Inst. of Technology, Dept. of Polymer Chemistry, Japan, 2/25  
Kyushu Univ., Dept. of Polymer Chemistry, Japan, 3/14  
Tokyo Univ., Dept. of Physics, Japan, 4/13  
Sony Research Center, Yokohama, Japan, 4/27  
Yamagata Univ., Yonezawa, Japan, 5/18  
Plenary Lecture, Society of Rheology, Tokyo, Japan, 5/19  
Nagayama Protein Array Project, Tsukuba, Japan, 5/26  
MITI Mechanical Engineering Laboratory, Tsukuba, Japan, 5/27  
Procter & Gamble Corp., Kobe, Japan, 6/2  
Kyoto Univ., Dept. of Polymer Physics, Uji, Japan, 6/7  
Osaka Univ., Dept. of Polymer Chemistry, Osaka, Japan, 6/9  
Inst. for Chemical Research, Uji, Japan, 6/14  
Univ. of Chicago, Physics Dept., 10/3  
Exxon Corp., Annandale, NJ, 11/8  
PPG Corp., Pittsburgh, PA, 11/10  
Medtronic Corp., Minneapolis, 11/14  
MRS Symp., Liquids in Confined Geometries, Boston, 12/1

#### 1995

Les Houches School of Physics, Soft Matter, France, 1/30  
Carnegie-Mellon Univ., Dept. Chem. Eng., Pittsburgh, PA, 1/28  
ACS Symp., Physical Chemistry of Polymers, Anaheim, CA, 4/3  
ACS Symp., Molecular Tribology, Anaheim, CA, 4/3  
Intl. Fine Particle Research Mtg., Urbana, IL, 6/14  
Adriatica Summer School, Physics of Friction, Trieste, Italy, 6/19  
Max-Planck-Institut für Kolloidforschung, Berlin, 6/27  
Intl. Workshop, Mechanisms in Tribology, Bar Harbor, Maine, 8/28  
AFOSR Tribology Workshop, Washington, DC, 9/21  
Exxon Research & Engineering, Annandale, NJ, 10/5  
Columbia Univ., Chem. Eng. Dept., New York, NY, 10/6  
Yale Univ., Chem. Eng. Dept., New Haven, CT, 11/6

Harvard Univ., Chem. Dept., Cambridge, MA, 11/8  
IBM Rüschlikon Lab., Zürich, Switzerland, 12/13  
ETH, Inst. für Polymere, Zürich, Switzerland, 12/15  
Max-Planck-Institut für Polymerforschung, Mainz, Germany, 12/18  
Institut für Mikromaschine, Mainz, Germany, 12/19

#### 1996

Northeastern Univ., Physics Dept., Boston, MA, 2/29  
Kansas State Univ., Physics Dept., Manhattan, KS, 3/7  
APS Symp., Confined Polymers, St. Louis, MO, 3/21  
Univ. Mass., Polym. Sci. Eng. Dept., Amherst, MA, 4/5  
Am. Cer. Soc. Symp., Basics of Processing, Indianapolis, IN, 4/15  
NSF Tribology Workshop, Richmond, VA, 4/16  
Cornell Univ., Chem. Eng. Dept., Ithaca, NY, 4/18  
Inst. of Tribology, Tsinghua Univ., Beijing, China, 5/13-15/96  
Dept. Mech. Eng., Zhe Zhiang University, Hangzhou, China, 5/20/96  
Dept. Precision Instruments, Jiatong Univ., Shanghai, China, 5/21/96  
NATO Conf. on Friction, Lisbon, Portugal, 6/20  
Gordon Conference on Tribology, New Hampshire, 7/1  
Argonne National Laboratory, Chicago, IL, 8/6  
ACS Symp., Polymer Interfaces, Orlando, FLA, 8/25  
Boston College, Chem. Dept., Boston, MA, 9/19  
Exxon Research & Engineering, Annandale, NJ, 9/23  
Univ. of Wisconsin, Dept. Chem. Eng., Madison, WI, 10/3  
Northwestern Univ., Dept. Materials Sci. Eng., Chicago, IL, 10/15  
MRS Symp., Dynamics in Small Confining Systems, Boston, MA, 12/2

#### 1997

Gordon Conference on Polymers, Ventura, CA 1/5  
Swiss Fed. Inst. Technology, Lausanne, Switzerland, 1/23  
3M Research, St. Paul, MN, 2/3  
Univ. North Carolina, Dept. Chemistry, Chapel Hill, NC, 2/27  
Harvard Univ., Dept. Applied Physics, Cambridge, MA, 3/7  
SRC/NIST Workshop on Polymer Interfaces, Gaithersburg, MD, 4/14  
Distinguished Visitors Program, NIST, Gaithersburg, MD, 4/15  
NSF Center for Polymers at Interfaces, Brooklyn, NY, 5/8  
AVS Meeting, Albuquerque, NM, 5/22  
Hitachi Corporate Research, Hitachi City, Japan, 6/6  
IFPRI International Meeting, Osaka, Japan, 6/9  
Japan/U.S. Polymers Conf., NIST, Washington, D.C., 6/18  
AFOSR Tribology Workshop, Dayton, OH, 6/24  
International Conference on Relaxations in Complex Systems, Vigo, Spain, 7/7  
Gordon Conference on Biomaterials, Holderness, N.H., 7/20  
European Conference on Confined Fluids, Lyon, France, 10/13  
NSF/Industry Symp. on MEMS Devices, Columbus, OH, 11/11

AIChE Symp. On Confined Fluids, L.A., CA, 11/16  
MRS Symp. on Polymer in Confined Spaces, Boston, MA, 12/1  
International Symp. on Dynamics of Liquids at Interfaces, Haifa, Israel, 12/14

J. Jonas:

Invited Talk, Symposium on Better Ceramics Through Chemistry VI, Materials Research Society Meeting, San Francisco, California, April, 1994.

Invited Talk, Steenbock Symposium on High Pressure Effects in Molecular Biophysics and Enzymology, Madison, Wisconsin, May 14-19, 1994.

Department of Chemistry, University of Adelaide, Adelaide, Australia, September 5, 1994.

Department of Chemistry, University of New South Wales, Australian Defense Force Academy, Canberra, Australia, September 12, 1994.

Department of Chemistry, Pennsylvania State University, University Park, Pennsylvania, September 27, 1994.

Lecturer in 1995 Lectureship Program of the Robert A. Welch Foundation:  
Texas Tech University, Lubbock, Texas, February 8, 1995  
University of Dallas, Irving, Texas, February 9, 1995  
University of Texas at Arlington, Arlington, Texas, February 10, 1995.

Invited Talk, Symposium on Protein Folding, American Physical Society, San Jose, California, March 22, 1995.

Invited Talk, Hitachi Advanced Research Laboratory, Tokyo, Japan, April 4, 1995.

NIST, Gaithersburg, Maryland, May 23, 1995.

Battelle Pacific Northwest Laboratories, Richland, Washington, July 11, 1995.

Invited Speaker, Joint XV AIRAPT & XXXIII EHPRG International Conference, Warsaw, Poland, September 11-15, 1995.

Medical Institute, University of Rio de Janeiro, Rio de Janeiro, Brazil, October 24, 1995.

Department of Biochemistry, University of Rio de Janeiro, Rio de Janeiro, Brazil, October



Workshop on Computational Experimental Approaches in Structural Biology, The Beckman Institute for Advanced Science and Technology, Urbana, Illinois, November 8, 1995.

Invited Speaker, Issues Conference: "Science and Technology" sponsored by the Senate Republican Conference, Washington, DC, March 25, 1996.

Invited Speaker, Thirteenth European Experimental N.M.R. Conference, La Villette, Cité des Sciences et de l'Industrie, Paris, France, May 19-24, 1996.

Invited Speaker, Maintaining America's Leadership in the 21st Century: "The Importance of Science and Technology Research" sponsored by the Senate Democratic Policy Committee Forum on Science and Technology, Washington, DC, June 19, 1996.

Invited Speaker, Symposium on Supercooled Liquids, ACS Meeting, Orlando, Florida, August 25-30, 1996.

Plenary opening lecture (Belgium Biophysical Society Lecture) at the XXXIVth Meeting of the European High Pressure Group. This meeting at the Katholieke Universiteit in Lueven Belgium, was held jointly with Japanese and European Seminars on Bioscience and Biotechnology, September 1-5, 1996.

Invited Speaker, Department of Biochemistry, College of Medicine, University of Illinois at Chicago, Illinois, March 20, 1997.

Invited Speaker, Protein Condensation Symposium, Rio De Janeiro, Brazil, May 25, 1997.

Invited Speaker, National Science Foundation, MPS Directorate, Arlington, Virginia, May 27, 1997.

Invited Speaker, AIRAPT-16 and HPCJ-38 Meeting on High Pressure Science and Technology, Kyoto, Japan, August 29, 1997.

Invited Speaker, Keihanna International Conference on Molecular Biophysics, Kyoto, Japan, August 31, 1997.

J. K. Shang:

**Technical Presentations:**

"Fluid-Assisted Microcrack Growth in  $\text{Si}_3\text{N}_4$ ," 18th Annual Conferences and Expo on Composites and Advanced Ceramics, Cocoa Beach, 1994.

"Contact Fatigue Damage in Ceramics," 18th Annual Conferences and Expo on Composites and Advanced Ceramics, Cocoa Beach, 1994.

"Fatigue Damage under Repeated Indentations," Am. Ceram. Soc. Annual Meeting, Cincinnati, 1994.

"Micromechanisms of High Temperature Fatigue Crack Growth in Ceramics," Int. Conf. Fracture Mechanics of Ceramics, Germany, 1995.

"Effect of Surface Roughness on Fatigue Crack Growth in Solder Joints," ASME Winter Meeting, San Francisco, 1995.

"Effect of Aging on Fatigue Crack Growth in Solder Joints," ASM Fall Meeting, Cleveland, 1995.

Keynote Lecture, Fatigue '96, May 1996, Berlin, Germany.

"Role of Grain Boundary Phase during Fatigue Crack Growth in Ceramics," TMS Annual Meeting, Orlando, 1997.

Visit: The Ford Scientific Research Lab, Dearborn, MI, May - July 1995.

#### D. Socie:

"Durability of Thick Thermal Barrier Coating," Engineering Foundation Conference, Switzerland, August 21-25, 1995.

Fracture Control Seminar (2 days), Helsinki University of Technology, Helsinki, Finland, May 29-June 2, 1995.

"Failure Strength and Mechanisms of a Woven Composite Laminate Under Multiaxial In-Plane Loading Durability and Damage Tolerance," ASME Winter Annual Meeting, December 10-14, 1994.

"Multiaxial Fatigue Damage," Fracture Control Program Short Course, University of Illinois, November 1-5, 1994.

"Statistical Strain-Life Fatigue Analysis," Society of Automotive Engineers, Detroit, Michigan, 1996.

"Fatigue Damage Simulation Models for Multiaxial Loading," Fatigue 96, Berlin, Germany, 1996.

"Durability of Thick Thermal Barrier Coatings" American Ceramics Society," Indianapolis, Indiana, 1996.

"Assessing Risk and Variability of Fatigue Lives in Cyclically Loaded Structures," Life assessment and Life Extension of Engineering Plant, Structures and Components, Cambridge, UK, 1997.

J. Hsia:

"Effect of Hydraulic Pressure on Surface Crack Propagation," presented at The International Symposium on Fracture and Strength of Solids, FEFG 1994, Xi'an, China, 1994.

"Effects of Crack Surface Morphology on the Fracture Behavior Under Mixed Mode Loading," presented at 27th ASTM National Symposium on Fatigue and Fracture Mechanics, Williamsburg, Virginia, June, 1995.

#### **4.2 Consultive/Advisory Functions**

A. J. Gellman

Professor Gellman made an informal visit to the fluids lubrication group at Wright Patterson AFB to exchange information regarding progress on the research supported by the URI which is being performed in parallel with projects at the WPAFB. Professor Gellman maintains contact with members of that group including Dr. H. Paige, Dr. P. John, and Dr. J. Liang. Materials have been supplied by WPAFB for use in Professor Gellman's work.

#### **4.3 Transitions**

A. J. Gellman:

Professor Gellman's expertise in tribology developed through AFOSR support over the past ten years has resulted in five examples of technology transitions. Expertise developed through the course of work on AFOSR funded projects has been brought to bear on several different problems. These collaborations have been in the form of funded research projects.

<u>Organization</u>	<u>Project Title</u>	<u>Support</u>	<u>Duration</u>	<u>Contact</u>
Hewlett-Packard Co.	Surface Chemistry of Fluorocarbons Lubricants on Ultra-smooth Media	\$158,000	1995-97	Mr. J. Ketchum
DOE Ames Lab	Quasicrystal Friction	\$42,000	1995-97	Prof. P.A. Thiel

<u>Organization</u>	<u>Project Title</u>	<u>Support</u>	<u>Duration</u>	<u>Contact</u>
Seagate Corp.	The Interaction of Fluoro-ether Lubricants with Modified Amorphous Carbon Films	\$50,000	1997-98	Dr. B. Marchon
Platinum Research Org.	Lubricant Development	\$50,000 (approved)	1997-98	Mr. C.F. Greer
National Storage Industries Consortium	Bonding of Fluoroether Lubricants to a-CH <sub>x</sub> and a-CN <sub>x</sub> Overcoats	\$25,000	1997	Ms. S. Rotter

## **5.0 INVENTIONS**

## **6.0 HONORS/AWARDS**

A. J. Gellman:

Alfred P. Sloan Research Fellow, A.P. Sloan Foundation 1991-93

Packard Fellowship in Science and Engineering  
David and Lucile Packard Foundation 1989-94

Beckman Fellow - Center for Advanced Study, University of Illinois 1989

Distinguished New Faculty in Chemistry Award  
Camille and Henry Dreyfus Foundation 1986

Arnold O. Beckman Research Award, U. of Illinois 1986

S. Granick:

Named to National Research Committee on Tribology, ASME, 1989.

Fellow, Center for Advanced Study, University of Illinois, 1990.

Fellow, American Physical Society, 1992.

Senior Xerox Award, University of Illinois, 1993.

Distinguished Polymer Lecturer, Lehigh University, 1993.

NSF Award for Special Creativity, 1993.

Sabbatical Scholar, Kyoto University, Japan, 1994.

Listed in Who's Who in Science and Engineering, 1995.

J. Jonas:

Member, National Academy of Sciences.

Fellow, American Academy of Arts and Sciences.

American Chemical Society Joel Hildebrand Award in the Theoretical and Experimental Chemistry of Liquids, 1983.

Fellow, American Association for the Advancement of Science.

Fellow, American Physical Society.

Fellow, American Institute of Chemists.

Senior U. S. Scientist Award from the Alexander von Humboldt Foundation of the Federal Republic of Germany, 1988.

University Senior Scholar, University of Illinois, 1985-1988.

Member, NRC Board on Chemical Science and Technology, 1997-2001.

Member, MPS Directorate Advisory Committee, National Science Foundation, 1997 -.